Journal of Power Sources 626 (2025) 235793

Contents lists available at ScienceDirect

Journal of Power Sources

journal homepage: www.elsevier.com/locate/jpowsour

(Fe, Co) oxide nanowires on gold nanoparticles modified MOF-derived carbon nanoflakes for high-efficiency sodium-ion batteries and supercapacitors across electrolytes

Hanxue Zhao [a,1], Wendong Xu [a,1], Mai Li [a,*], Zheyi Meng [b], Inaam Ullah [a], Muhammad Zubair Nawaz [c], Jiale Wang [a], Chunrui Wang [a], Paul K. Chu [d]

[a] College of Science, Donghua University, Shanghai, 201620, China
[b] State Key Laboratory for Modification of Chemical Fibers and Polymer Materials, College of Material Science, Donghua University, Shanghai, 201620, China
[c] Southern University of Science and Technology, Shenzhen, China
[d] Department of Physics, Department of Materials Science and Engineering, and Department of Biomedical Engineering, City University of Hong Kong, Tat Chee Avenue, Kowloon, China

HIGHLIGHTS

- 1.Au nanoparticles and ZnCo-MOF Derived CPCN integration: Enhances surface electron transport for superior performance.
- Flexible electrode: Introduces a flexible electrode (FCO/Au/CPCN@CC) that boosts catalytic activity in a limited space.
- Superior supercapacitor performance: AC//FCO/Au/CPCN@CC exhibits excellent power density and capacitance retention.
- Enhanced characteristics in sodium-ion batteries: Features high specific discharge capacity and good stability.
- Strong sodium-ion adsorption: DFT reveals impressive sodium-ion adsorption for FCO/Au/CPCN@CC.

GRAPHICAL ABSTRACT

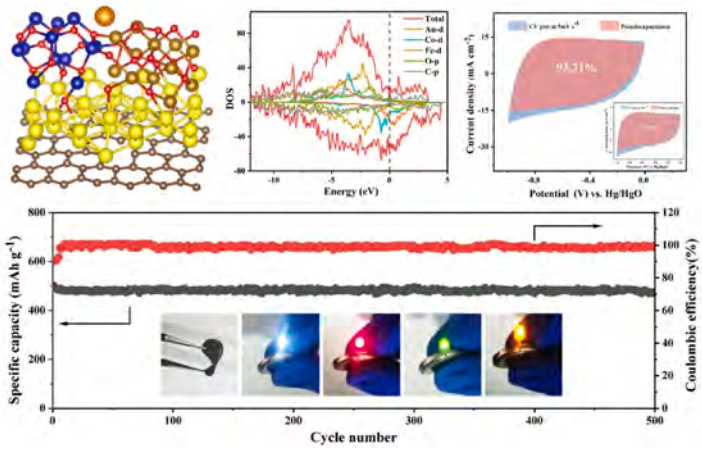

ARTICLE INFO

Keywords:
(Fe, Co) oxide nanowires
Porous carbon nanosheets
Supercapacitors
Sodium-ion batteries
Gold nanoparticles

ABSTRACT

The three-dimensional conductive porous carbon nanosheets (CPCN) are from the bimetallic metal-organic framework (MOFs) consisting of organic ligating groups that incorporate zinc and cobalt ions deposited onto a flexible carbon cloth (CC). Utilizing a hydrothermal approach, iron-cobalt oxide (FCO) nanowires are intricately embedded onto CPCN modified with gold (Au), forming a flexible FCO/Au/CPCN@CC electrode. The electrochemical characteristics of electrodes are evaluated in 1 M Na_2SO_4, supercapacitor's storage capacity is tested at 4 V using 1 M $NaPF_6$ electrolyte. Among its remarkable attributes are a peak energy density of 291.5 W

* Corresponding author.
E-mail address: limai@dhu.edu.cn (M. Li).
[1] These authors contributed equally to this work.

https://doi.org/10.1016/j.jpowsour.2024.235793
Received 14 June 2024; Received in revised form 23 September 2024; Accepted 4 November 2024

h kg^{-1} achieved at a power density of 153.85 W kg^{-1}, and even at the maximum power density of 1749.9 W kg^{-1}, it maintains 144.78 W h kg^{-1}. Undergoing 10,000 rounds of GCD, the equipment sustains a capacitance retention of 84.27 %. Moreover, the performance of the FCO/Au/CPCN@CC anode in sodium-ion batteries (SIBs) is assessed. At 0.1C, the discharge capacity reaches 958 mAh g^{-1}, and there is almost no loss after the rate cycle. The Coulomb efficiency surpasses 98 % during 500 cycles at a large C-rate. The integration of Au nanoparticles onto the CPNC surface enhances the energy storage characteristic of the FCO/Au/CPCN@CC composite material in both battery and supercapacitor applications.

1. Introduction

Due to the urgency of energy sustainability and environmental protection, there is a significant requirement for environmentally friendly energy storage solutions [1–3]. Although rechargeable batteries and supercapacitors are prevalent in green electrochemical storage, the advent of new energy vehicles and advanced technologies demand batteries with enhanced energy storage capabilities [4]. To meet the increasing demand, integrating supercapacitor electrode technology into batteries can improve the storage capability [5]. However, current research on supercapacitor electrodes for battery energy storage is limited. Using the same electrode materials has the potential to boost the performance of both supercapacitors and batteries representing a novel research direction in energy storage technology. Traditional batteries often prioritize electrode designs optimized for energy densities, while potentially neglecting the power output [6]. By incorporating electrodes catering to supercapacitors (SCs) with excellent charging-discharging rates, the power density of batteries can be improved [5,7]. Both supercapacitors and batteries can be integrated to form an energy storage system (ESS) that maximizes the utility of both power and energy. The key objective here is to amplify their respective strengths while minimizing their shortcomings. The energy storage system for sodium ions (including batteries and supercapacitors) has many advantages like faster charging speed, suitable for fast response storage systems and a longer cycle life can meet the needs of long-term storage. This strategy paves the way for innovative battery technology that balances the high energy capacity with rapid energy discharging and recharging, consequently bridging the gap between the two devices [8].

Owing to the high charging and discharging rates, extended lifespan, as well as transmission power, SCs are among the foremost devices for energy storage [9–11]. Derived from the underlying charge storage principles, supercapacitors (SCs) include pseudocapacitors and electric double-layer capacitors (EDLCs) [12,13]. Because of the rapid and reversible redox reaction, pseudocapacitors generally possess superior energy density and specific capacitance than EDLCs [14,15]. The electrode material and structure are paramount in defining the efficacy of SCs [16,17]. Consequently, recent research on supercapacitors has primarily centered around advancing redox active materials for pseudocapacitors with good stability capacitance and high specificity [9]. Electrode materials commonly used in electrochemical energy stores include transition metal oxygenates, conductive polymers as well as carbonaceous materials [18–21]. Specifically, transition metal oxides have been thoroughly explored for their advantageous capacitance properties, such as their elevated specific capacity, controllable morphology, and cost-effectiveness [22]. Among the diverse array of transition metal oxides, iron and cobalt oxides emerge as the preferred choices for electrodes in supercapacitors, on account of their notable theoretical specific capacity, cost-effectiveness, together with excellent stability [23–25]. In particular, Chen et al. [26] disclosed an α-Fe_2O_3/C tetsubo-like structure exhibiting a capacity of 391.8 F g^{-1} at 1 mA cm^{-2}. Co_3O_4@C nanosheets were prepared by Gong et al. [27], demonstrating a capacitance of 251 F g^{-1} at 1 A g^{-1}. In spite of that the low electrical conductivity hindered the practical application of iron and cobalt oxides [28]. To solve this problem, metal oxides and conductive carbonaceous materials can be combined [29], and the synergistic interplay between the components in hybrid materials can enhance the electrochemical properties [30].

Metal-organic framework (MOFs) are a sort of crystalline porous materials comprising inorganic metal sites coordinated with organic chelators. They have the advantage of controllable morphology, thus allowing the precise synthesis of carbonaceous materials with tailored structures boasting superior electrical conductivity, adjustable porosity, vast surface area, and good stability [31]. Hence, bimetallic MOFs have garnered considerable research interest as a result of their exceptional electrical conductivity, robust structural stability, and easy synthesis [32]. Liang et al. [33] have used a hydrothermal method to prepare Ni_nCo_mMOFs exhibiting a layer-and-channel architecture. The capacitance of Ni_1Co_1MOF is 1333 F g^{-1} at 2 A g^{-1} (Ni_1Co_1MOF//AC presenting a peak energy density of 28 Wh/kg at 444 W kg^{-1}), It surpasses the capacitance exhibited by the single-metal MOF (Ni-MOF and Co-MOF). Lim et al. [34] have synthesized $ZnCo_2O_4$ from bimetallic cobalt-based MOFs. Compared with Co_3O_4 derived from MOF, the specific capacity of the bimetallic oxide increases by more than 300 % besides enhanced stability. Bimetallic MOFs can function as the precursors/templates for fabricating diverse nanocomposites [35–37]. Similar to bimetallic MOFs, bimetallic oxides and hydroxides have been demonstrated for their synergistic characteristics in developing electrode materials for charge storage applications. Indeed, these electrode materials made of heterometallic compositions can exhibit much improved electrochemical performance over that of single metal compounds. For instance, CPCN derived from MOFs can serve as efficient materials for producing high-performance electrodes [38,39].

A novel flexible FCO/Au/CPCN@CC electrode has been creatively created and shown in this ground-breaking study for use in sodium-ion batteries and supercapacitors. The procedure entails the accurate and uniform development of iron-cobalt oxide nanowires on flexible conductive porous carbon nanosheets that have been altered with gold, as illustrated in Fig. 1. The procedure involves the continuous application of ZnCo-MOFs sheets onto the surface of carbon cloth after plasma treatment, followed by carbonization and etching to create the CPNC@CC structure. Before actively depositing the material, gold nanoparticles are applied to the flexible CPCN, which increases the surface area and improves the assimilation of active chemicals as well as conductivity [40,41]. The FCO/Au/CPCN@CC electrode demonstrates superior electrochemical characteristics compared to other electrode configurations such as FCO/CC, Fe_2O_3/CPCN@CC, and FCO/CPCN@CC. These electrodes were all manufactured using a comparable approach. The comparison was conducted in a 1 M Na_2SO_4 environment. An asymmetrical supercapacitor (ASC) is constructed utilizing FCO/Au/CPCN@CC, active carbon (AC), and 1 M Na_2SO_4 as the electrolyte for operation in the 2 V window (AC//FCO/Au/CPCN@CC-2V), which showed outstanding operational efficiency. To further demonstrate its capabilities, a flexible ASC with the identical electrode combination the AC is assembled with 1.0 M $NaPF_6$ for the 4 V window (AC//FCO/Au/CPCN@CC-4V).

Regarding anode materials utilized in SIBs, FCO/Au/CPCN@CC not only have favorable sodium storage properties but also leverage a large power density inherent to supercapacitor electrodes. A button battery is assembled with FCO/CPCN@CC and FCO/Au/CPCN@CC as the working electrodes, sodium sheet fulfills the role of the auxiliary electrode in a 1.0 M $NaPF_6$ solvent. The sodium storage characteristics are studied in a 3 V window. The research demonstrates improved storage capacity in

SIBs by utilizing the distinctive electrode structure and optimizing the process.

2. Experiments and approaches

2.1. Materials synthesis

The preparation of FCO/Au/CPCN@CC is illustrated in Fig. 1. A 45 mL solution of deionized (DI) water containing 0.6 mM $Zn(NO_3)_2{\cdot}6H_2O$ and 1.3 mM $Co(NO_3)_2{\cdot}6H_2O$ was prepared. Subsequently, a 45 mL solution of composed of DI water infused with dissolved 2-methylimidazole was introduced into the mixture and stirred magnetically. Soaked the clean carbon cloth after plasma treatment for 3 h, washed, and dried to produce ZnCo-MOF@CC. It underwent a 2-h annealing process at 950 °C in a nitrogen-filled atmosphere. To eliminate Co^{2+}, Zn^{2+}, and other contaminants, a second thermal treatment is applied in 6 M HNO_3 at 100 °C for 24 h, resulting in the fabrication of flexible CPCN@CC.

To modify the flexible CPCN@CC substrate with gold nanoparticles (AuNPs), a round-bottom flask containing 2 ml of 1.3 mM PVP and 2 ml of 34.0 mM $C_6H_5Na_3O_7{\cdot}2H_2O$ together with 96 ml of water was introduced while heated and stirred. When the mixture starts to boil, add 250 μL of 100 mM $HAuCl_4{\cdot}3H_2O$ and CPCN@CC, and heat for half an hour. The reaction has concluded, yielding Au/CPCN@CC.

The FCO composite was fabricated on CPCN@CC, CC, and Au/CPCN@CC hydrothermally. A solution of DI water with ethylene glycol was stirred after the addition of 1.5 mM $Co(No_3)_3{\cdot}6H_2O$, 1.5 mM $Fe(NO_3)_2{\cdot}9H_2O$, 15 mM urea, and 3.9 mM NH_4F. Transfer the mixture to a reactor containing Au/CPCN@CC, CC, or CPCN@CC and subsequently heat for approximately 8 h at 120 °C. Then the sample is annealed in 350 °C air for 2 h to obtain FCO/CC, FCO/CPCN@CC, and FCO/Au/CPCN@CC. The Fe_2O_3/CPCN@CC electrode was fabricated following identical procedures, excluding the inclusion of $Co(No_3)_3{\cdot}6H_2O$.

2.2. Materials characterization

The electrodes' morphology, microstructure, as well as constituent elements were evaluated using scanning electron microscopy (SEM, Hitachi S-4800, Japan), microstructure, and elemental constitution of the electrodes, selected-area electron diffraction (SAED, Oxford Instruments X-MAX 80TLE, England), energy-dispersive X-ray spectroscopy (EDS, JEOL JEM 2100F, Japan), and transmission electron microscopy (TEM, JEOL JEM 2100F, Japan, 200 kV). The crystalline phase was observed by X-ray diffraction (XRD) with RigakuD/max-2550VB+/PC, and X-ray photoelectron spectroscopy (XPS) with Thermo Fisher ESCALB 250XI to determine the chemical states and composition.

2.3. Electrochemical assessment

A three-electrode apparatus employing 1 M Na_2SO_4 was set up on the CHI660E electrochemical workstation. Five electrode materials were evaluated for comparison, including FCO/Au/CPCN@CC, FCO/CPCN@CC, FCO/CC, Fe_2O_3/CPCN@CC, and Au/CPCN@CC. The reference electrode was the saturated calomel electrode, while the counter electrode was comprised of platinum wire. To ascertain the electrochemical behavior, Cyclic Voltammetry (CV), Galvanostatic Charging/Discharging (GCD), and Electrochemical Impedance Spectroscopy (EIS) measurements were conducted. The asymmetrical supercapacitor device incorporated both an aqueous system utilizing 1.0 M Na_2SO_4 solution and an organic system employing a 1.0 M $NaPF_6$ solution. The sodium-ion batteries consisted of FCO/Au/CPCN@CC or FCO/CPCN@CC as the electrode, as a reference electrode, sodium metal foil was employed, while glass fiber worked as the isolator in 1.0 M $NaPF_6$ solution. The charging/discharging test was performed in a 3 V voltage window on the NEWARE BTS battery system under various C-rates (1 C = 1000 mAh g^{-1}). CV was executed on the CHI660E electrochemical workstation.

Eqs. (1)–(3) were employed for calculating the specific capacitance (Cs), energy (E) density, as well as power density (P) of the electrodes [42]:

$$c_s = \frac{I \times \Delta t}{m \times \Delta V} \tag{1}$$

$$E = \frac{C \times (\Delta V)^2}{2 * 3.6} \tag{2}$$

$$P = \frac{E*3600}{\Delta t} \tag{3}$$

2.4. Theoretical evaluation

First-principles calculations [43,44] were conducted employing spin-polarized density-functional theory (DFT) within the framework of the generalized gradient approximation (GGA) by the Perdew-Burke-Ernzerhof (PBE) [45]. Projected augmented wave (PAW) potentials are used to represent ionic nuclei [46,47], and the kinetic energy cut-off of the valence electrons is 450eV. Using Gaussian fitting, the occupied width of the Kohn-Sham orbit is 0.1eV. The electronic energy was considered to have reached equilibrium once the energy change fell below 10^{-5} eV. Similarly, the geometric optimization was

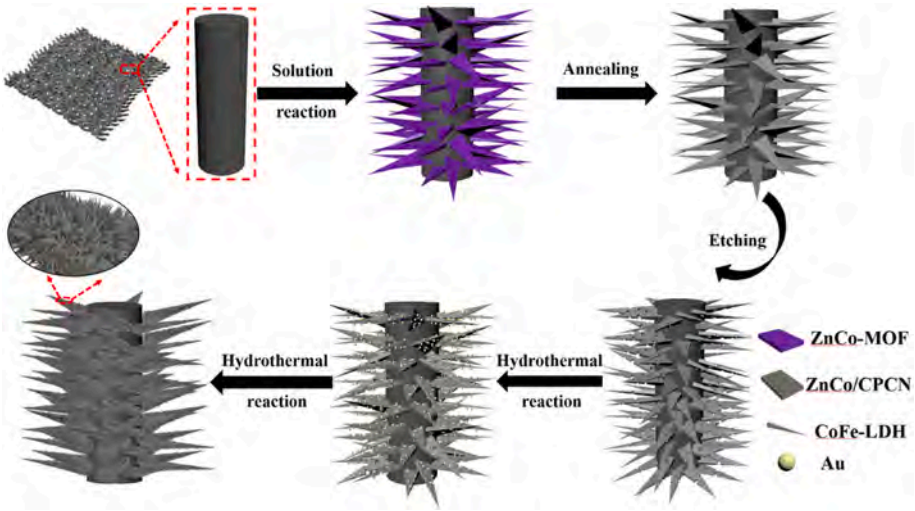

Fig. 1. Schematic illustration of the fabrication of the electrodes.

deemed to have converged once the force variation was reduced to below 0.02 eV/Å. Dispersive interactions are illustrated using grime's DFT-D3 method [48]. The adsorption energy (E_{ads}) about Na is designated as:

$$E_{ads} = E_{Na/surf} - E_{surf} - E_{Na(g)}, \quad (4)$$

Where $E_{Na/surf}$ signifies the energy associated with the adsorption of Na onto the surface, Esurf denotes the energy of the surface when it is not adsorbed, and $E_{Na(g)}$ indicates the energy of an isolated Na molecule situated in a cube with a side of 20 Å, utilizing a 1 × 1 × 1 Monkhorst-Pack k-point grid for Brillouin zone sampling.

3. Findings and analysis

3.1. Materials analysis

Fig. 2 together with Fig. S1 are Scanning Electron Microscope (SEM) micrographs. ZnCo-MOF nanosheets are evenly coated on CC substrate, as illustrated in Figs. S1(a)–(b). The thickness of the three-dimensional structure varies between 120 and 170 nm. After high-temperature annealing, the ZnCo-MOF sheets exhibit a noticeable reduction in thickness of approximately 50 nm, as shown in Fig. 2(a) and (b). The formation of the 2D conductive porous carbon nanosheets involves annealing and carbonization of the MOF nanosheets, followed by etching to create hollow structures on carbon cloth (Fig. 2(c) and (d)). The annealing step augments the durability and binding of the MOF precursor with the CC, ensuring the preservation of the precursor's structural integrity following the hydrothermal reaction. High-temperature annealing repairs the weak bonds or defects in the precursor structure, resulting in a more stable and robust MOF framework. Additionally, annealing promotes better adhesion between the MOF and CC by facilitating molecular interactions and surface diffusion, thereby enhancing the binding strength and reducing the likelihood of delamination or detachment during subsequent processing. The CPCN@CC nanocomposite's specific surface area is augmented due to the thinner nanosheets and void structures within it. In Fig. 2(e) and (f), gold nanoparticles with a diameter of approximately 20 nm are deposited on CPCN@CC. The combination of AuNPs with CPCN enhances the conductivity and contact area. The nanoscale Fe_2O_3 particles are evenly dispersed on the CPCN@CC substrate, as shown in Fig. 2(g) and (h). For experimental validation, iron-cobalt oxide (FCO) is grown directly on carbon cloth (CC) (Fig. 2(i) and (j)), and the images reveal nanowire arrays on the carbon fibers with lengths of several micrometers and diameters ranging from 500 to 700 nm. FCO nanowires are evenly distributed on the Au/CPCN@CC in Fig. 2(k) and (l). The unique nanowire structure with CPCN facilitates swift reaction kinetics, enhancing the efficiency of redox reactions.

Fig. 3(a) displays the X-ray Diffraction (XRD) datas of ZnCo-MOF, CPCN@CC, Au/CPCN@CC, Fe_2O_3/CPCN@CC, FCO/CPCN@CC, and FCO/Au/CPCN@CC. The Co and Zn diffraction peaks seen in the ZnCo-MOF sample (depicted in black) match the findings reported in prior literature confirming the successful fabrication of ZnCo-MOF. The etching process eliminates Zn and Co from the ZnCo-MOF precursors, thus resulting in the CPCN@CC sample (depicted in red) exhibiting no observable Co or Zn peaks. The Au peaks in the Au/CPCN@CC (orange) as well as FCO/Au/CPCN@CC (purple) spectra, located at 64.58°, 44.39°, 38.18° and, originating from the (220), (200), and (111) lattice planes of gold, as referenced in the PDF#04–0784 database. Fe_2O_3/CPCN@CC (blue), FCO/CPCN@CC (green), and FCO/Au/CPCN@CC (purple) show peaks of Fe_2O_3 at 18.00°, 24.61°, 35.09°, 37.87°, 53.62°, 56.64°, 58.83°, and 64.91° associated with the (102), (017), (201), (0015), (300), (0217), (309), and (226) planes of Fe_2O_3 (PDF#40–1139), respectively. FCO/CPCN@CC (green) and FCO/Au/CPCN@CC (purple) exhibit peaks of Co_3O_4 at 31.27°, 36.85°, and 44.81°, associating with the (220), (311) and (400) crystalline phase of PDF#42–1467, respectively.

Two distinct peaks are observed in Fig. 3(b), belonging to Au $4f_{5/2}$ at 84.1eV and Au $4f_{3/2}$ at 87.8eV, which corresponds to earlier research [49]. The XPS spectrum for Co2*p* is depicted in Fig. 3(c). 786 eV and 806.92 eV are the two satellite spikes, Co $2p_{3/2}$ at 781eV is one of the two major summits, while Co $2p_{1/2}$ at 796.1eV is the other. These

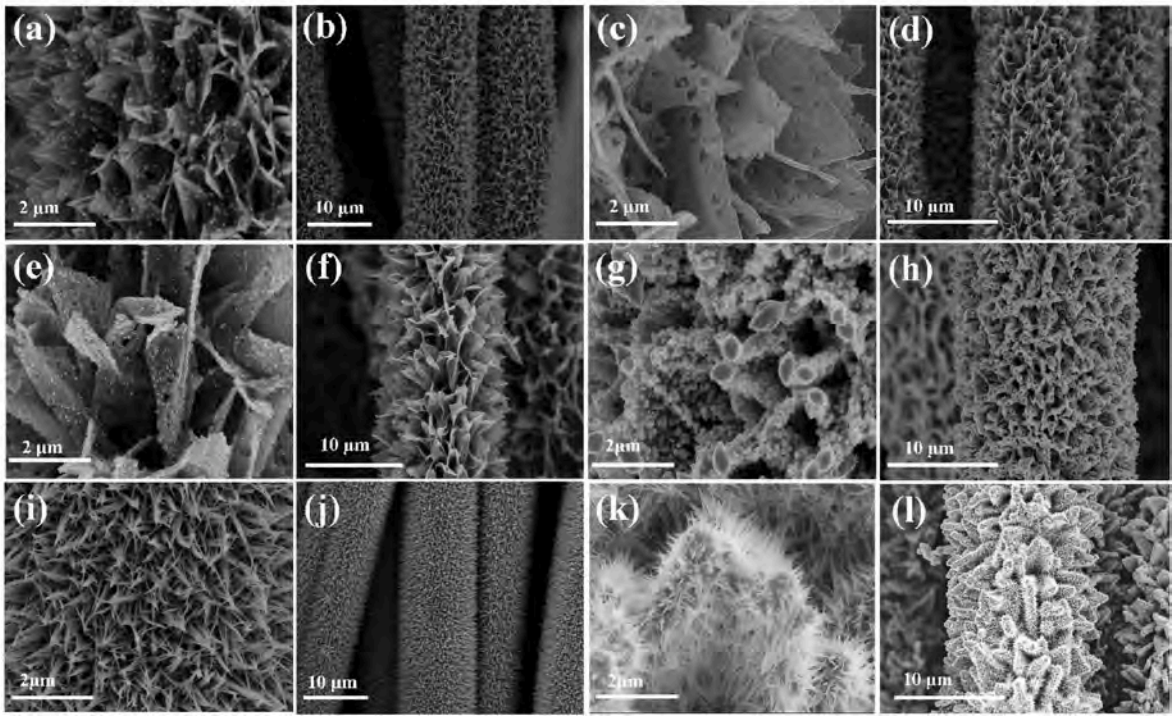

Fig. 2. SEM images: (a, b) ZnCo-MOF after annealing, (c, d) ZnCo-MOF after etching (CPCN@CC), (e, f) Au/CPCN@CC, (g, h) Fe_2O_3/CPCN@CC, (i, j) FCO/CC, and (k, l) FCO/Au/CPCN@CC.

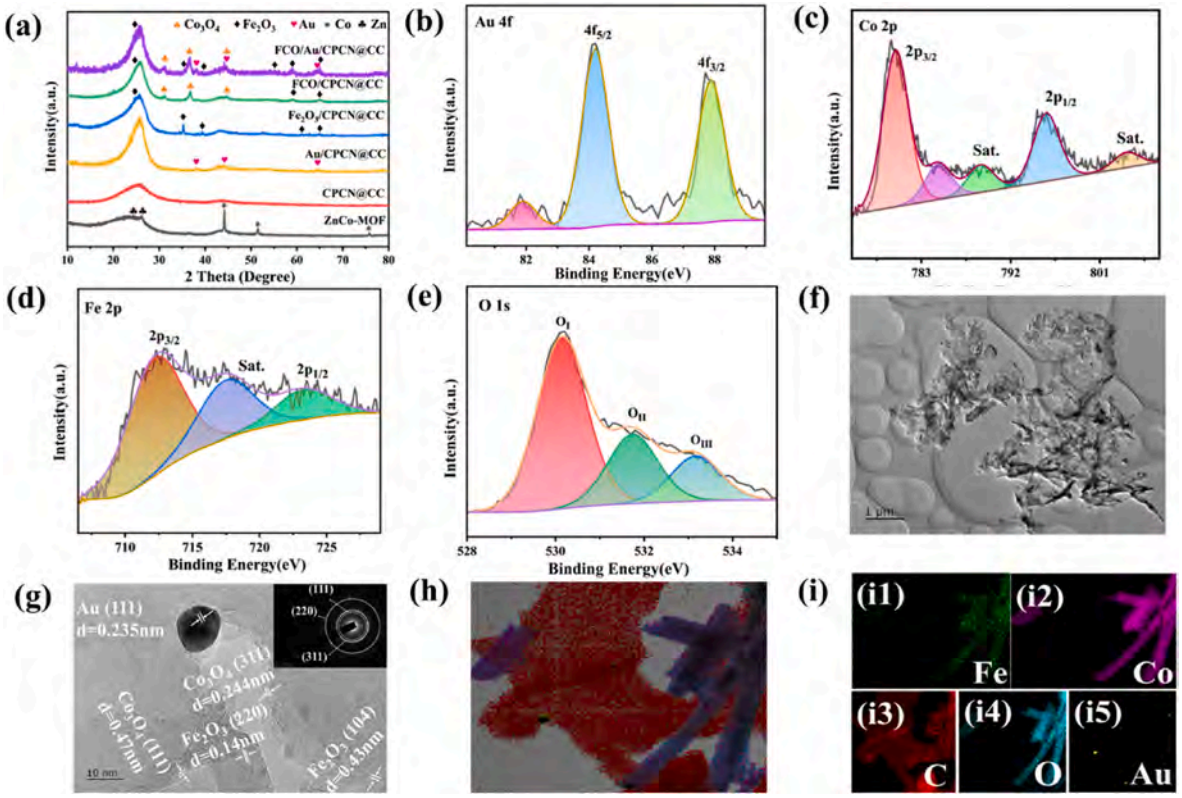

Fig. 3. (a) XRD spectra of ZnCo-MOF, CPCN@CC, Au/CPCN@CC, Fe_2O_3/CPCN@CC, FCO/CPCN@CC and FCO/Au/CPCN@CC; XPS spectra of (b) Au 4*f*, (c) Co 2*p*, (d) Fe 2*p*, and (e) O 1*s*; (f, g) TEM and HR-TEM images of FCO/Au/CPCN@CC; (h) EDS elemental maps of FCO/Au/CPCN@CC; (i1) EDS Fe map, (i2) EDS Co map, (i3) EDS C map, (i4) EDS O map, and (i5) EDS Au map.

findings suggest the presence of Co^{2+} and Co^{3+}states in Co_3O_4 [50,51]. Fe^{3+} in Fe_2O_3 has a Fe $2p_{1/2}$ summit at 724.9eV, a Fe $2p_{3/2}$ summit at 711.2 eV, as well as a satellite summit at 717.5 eV (Fig. 3(d)) [14,16]. Fig. 3(e) shows three distinct component peaks in the O 1*s* spectrum. The summit situated at 529.8 eV (O_I) matches with lattice oxygen, The 531.8eV peak (O_{II}) correlates with hydroxyl oxygen, and the peak at 533.5 eV (O_{III}) aligns with physically adsorbed oxygen [49,52,53]. Fig. S8(a) depicts the C1s core-level spectrum of FCO/Au/CPCN@CC, featuring three prominent peaks corresponding to C=O at 286.7 eV, C-C/C=C at 284.3 eV, and C-O at 285.6 eV. Additionally, the N1s core-level (Fig. S8(b)) spectrum exhibits peaks attributed to N-H at 400.4 eV and C=N at 398.9 eV.

The morphology and microstructure of the composite are characterized and analyzed through Transmission Electron Microscopy (TEM) as shown in Fig. 3(f) and (g). High-resolution TEM reveals a lattice interval of 0.235 nm aligns with the (111) phase of Au, 0.47 and 0.244 nm accords with the Co_3O_4 (111) and (311) phase, as well as 0.14 and 0.43 nm for the Fe_2O_3 (220) and (104) phase, respectively. The SAED diagram (inset in Fig. 3(g)) verifies the successful assembly of the Au particles and FCO. The EDS elemental maps in Fig. 3(h) and (i) show gold particles, FCO nanowires, and homogeneous Fe, Co, C, O, and Au distributions. The results corroborate the fabrication of the materials. The specific information of the lattice lines, Fast Fourier Transform (FFT) and Inverse Fast Fourier Transform (IFFT) patterns in Fig. 3(g) is included in Supporting Information Fig.S10.

3.2. Electrochemical properties

The composite materials' characteristics were assessed in a 1M Na_2SO_4 solution employing a three-electrode setup, which saturated calomel electrode ($Hg/HgCl_2/KCl$) was the reference electrode and platinum wire was the counter electrode. In Fig. 4(a) and (b), the electrochemical features of Fe_2O_3/CPCN@CC, Au/CPCN@CC, FCO/Au/CPCN@CC, FCO/CPCN@CC, as well as FCO/CC are similar. However, The FCO/Au/CPCN@CC exhibits an extended discharge duration, with a correspondingly larger CV area compared to that of Au/CPCN@CC, FCO/CPCN@CC, FCO/CC, and Fe_2O_3/CPCN@CC. The electrochemical behaviors of the FCO/CPCN@CC and FCO/Au/CPCN@CC electrodes were analyzed in the frequency range of 0.01–100 kHz using electrochemical impedance spectroscopy (EIS) for further assessment of the electrode materials (Fig. 4(c)). The impedance data were fitted with an equivalent circuit model using Z-view software. At high frequencies, the X-intercept indicates the electrolyte resistance (R_s), while the semicircle corresponds to the charge transfer resistance (R_{ct}). Warburg impedance (W_o) is used to characterize the diffusion processes of substances within electrodes or electrolytes. It typically appears as a skewed straight line in the impedance spectrum, particularly in the low-frequency region. Additionally, a constant phase element (CPE) is often employed in place of an ideal capacitor to better represent the non-homogeneous characteristics of the system. The resistance values for both electrodes are summarized in Table S2. For the FCO/Au/CPCN@CC electrode, the calculated R_s is 5.18Ω, whereas the R_s for the FCO/CPCN@CC electrode is 6.52Ω. The lower intrinsic resistance of the FCO/Au/CPCN@CC electrode suggests it has better conductivity. The FCO/Au/CPCN@CC electrode demonstrates a lower charge transfer impedance (R_{ct} = 0.42 Ω) compared to the bimetallic FCO/CPCN@CC electrode (R_{ct} = 1.14 Ω). Hence, the FCO/Au/CPCN@CC electrode outperforms the bimetallic FCO/CPCN@CC electrode in energy storage processes, exhibiting superior capacitance characteristics and faster electron/ion transport.

Fig. 4(d) gives the Cyclic Voltammetry (CV) data of FCO/Au/CPCN@CC, revealing consistently similar shapes that gradually increase with increasing scan speeds, thus demonstrating favorable capacitive characteristics and outstanding rate performance [54]. Galvanostatic Charge-Discharge (GCD) data in Fig. 4(e) depicts an almost symmetrical

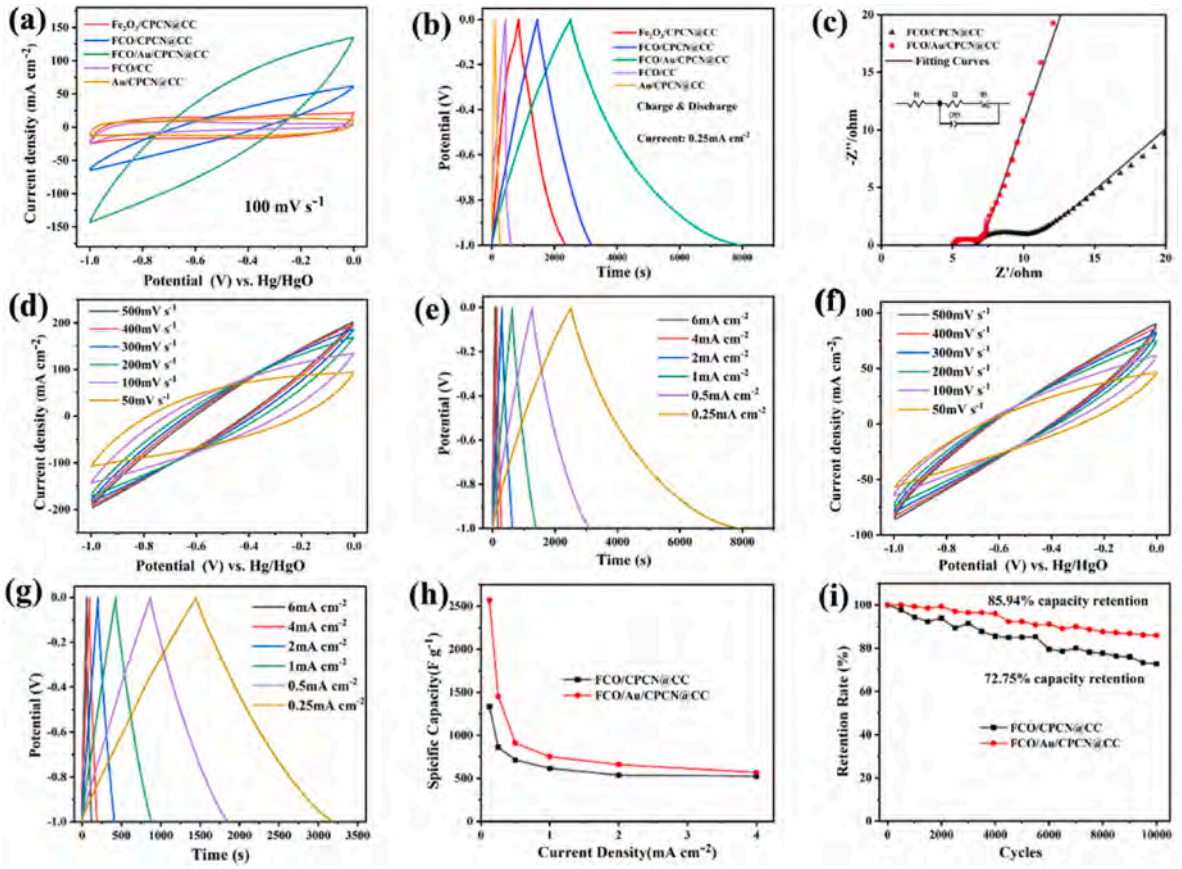

Fig. 4. (a) CV curves at 100 mV s^{-1} and (b) 0.25 mA cm^{-2}: GCD curves of Fe_2O_3/CPCN@CC, FCO/CPCN@CC, FCO/Au/CPCN@CC, FCO/CC and Au/CPCN@CC; (c) Nyquist plots of FCO/CPCN@CC and FCO/Au/CPCN@CC; (d) CV curves and (e) GCD curves of FCO/Au/CPCN@CC; (f) CV curves and (g) GCD curves of FCO/CPCN@CC; (h) Specific capacities for different current densities and (i) Cycle stability at a GCD current density of 5 mA cm^{-2} of FCO/CPCN@CC and FCO/Au/CPCN@CC.

triangular structure across various current densities, indicative of the desired electrochemical capacitive performance and rapid faradaic redox kinetics. In comparison, the CV curves of FCO/CPCN@CC (Fig. 4 (f)) exhibit a smaller rectangular area at the same scanning speed, while the GCD curves (Fig. 4(g)) show a shorter charging time at the same current densities. According to Fig. 4(e) and (g), and Eq. (1), the capacitance is obtained (Fig. 4(h)). Remarkably, at 0.25 mA cm^{-2}, the capacitance of FCO/Au/CPCN@CC is 2570.09 F g^{-1}, while FCO/CPCN@CC is only 1335 F g^{-1} under identical current density. The outcomes surpass those of rGO/Co_3O_4@Fe_2O_3 (784 F g^{-1}) [27], α-Fe_2O_3/C (391.8 F g^{-1}) [26], and nanowire $FeCo_2O_4$ (1963 F g^{-1}) [55]. Fig. 4(i) demonstrates the durability of FCO/CPCN@CC as well as FCO/Au/CPCN@CC through 10000 cycles, and FCO/Au/CPCN@CC maintains a capacitance retention of 85.94 % surpassing that of 72.75 % of FCO/CPCN@CC. The SEM images of FCO/Au/CPCN@CC after 10000 cycles are exhibited in Fig. S11. It is clearly shown that the morphology has changed. However, the composite structure of FCO/Au/CPCN@CC is still retained, which also proves that the sample has high electrochemical stability.

To analyze the energy accumulation process of the FCO/CPCN@CC and FCO/Au/CPCN@CC electrodes, in conformity with the CV data in Fig. 5(a), k_1 (Fig. 5(b) and (c)) [56] via eq. (5) obtained the pseudocapacitance:

$$i(V) / v^{1/2} = k_1 v^{1/2} + k_2, \quad (5)$$

The scanning rate is represented by v, while k_1 corresponds precisely to the inclination or gradient of the curves depicted in Fig. 5(b) and (c) $k_1 v$ affects the pseudo capacitance current at different voltages. i (V) signifies the current at a voltage. Fig. 5(d) illustrates the pseudocapacitance contribution (represented by the pink area). The percentages of the pseudo-capacitance contribution under various scanning speeds are consolidated in Fig. 5(e) and (f). Fig. 5(d) displays the ratio of pseudocapacitance of FCO/CPCN@CC. At 1 mV s^{-1}, the proportion of FCO/CPCN@CC is 73.07 %. At 5 mV s^{-1}, the proportion reaches 87.45 %. Fig. 5(f) gives the relative contribution of pseudocapacitance for the FCO/Au/CPCN@CC electrode across various scanning rates. Notably, FCO/Au/CPCN@CC exhibits a greater pseudocapacitance contribution than FCO/CPCN@CC. As an example, FCO/Au/CPCN@CC exhibits a pseudocapacitance ratio of 93.31 % at 5 mV s^{-1}, outperforming FCO/CPCN@CC's 87.45 % ratio under the same scanning conditions. Fig. 5(g) exhibits the in-situ XRD of FCO/Au/CPCN@CC.

The overall X-ray diffraction peak shape and intensity of characteristic peaks of the material did not show significant changes, indicating that FCO/Au/CPCN@CC can maintain its original crystal structure over such a long period of time, proving its high stability. Simultaneously, it signifies that the processes taking place in a 1M Na_2SO_4 solution do not constitute an oxidation-reduction reaction, but instead, they involve the surface adsorption and desorption of sodium ions. The enhanced surface area of FCO/Au/CPCN@CC facilitates increased ion interaction, thereby improving the efficiency of charge transfer processes during ion intercalation. This enlarged interface is pivotal in accelerating the rate of ion intercalation and refining the charge storage mechanism of FCO/Au/CPCN@CC, consequently resulting in superior electrochemical performance relative to FCO/CPCN@CC.

3.3. *FCO-based flexible supercapacitors*

To further demonstrate the diverse application potential, asymmetric

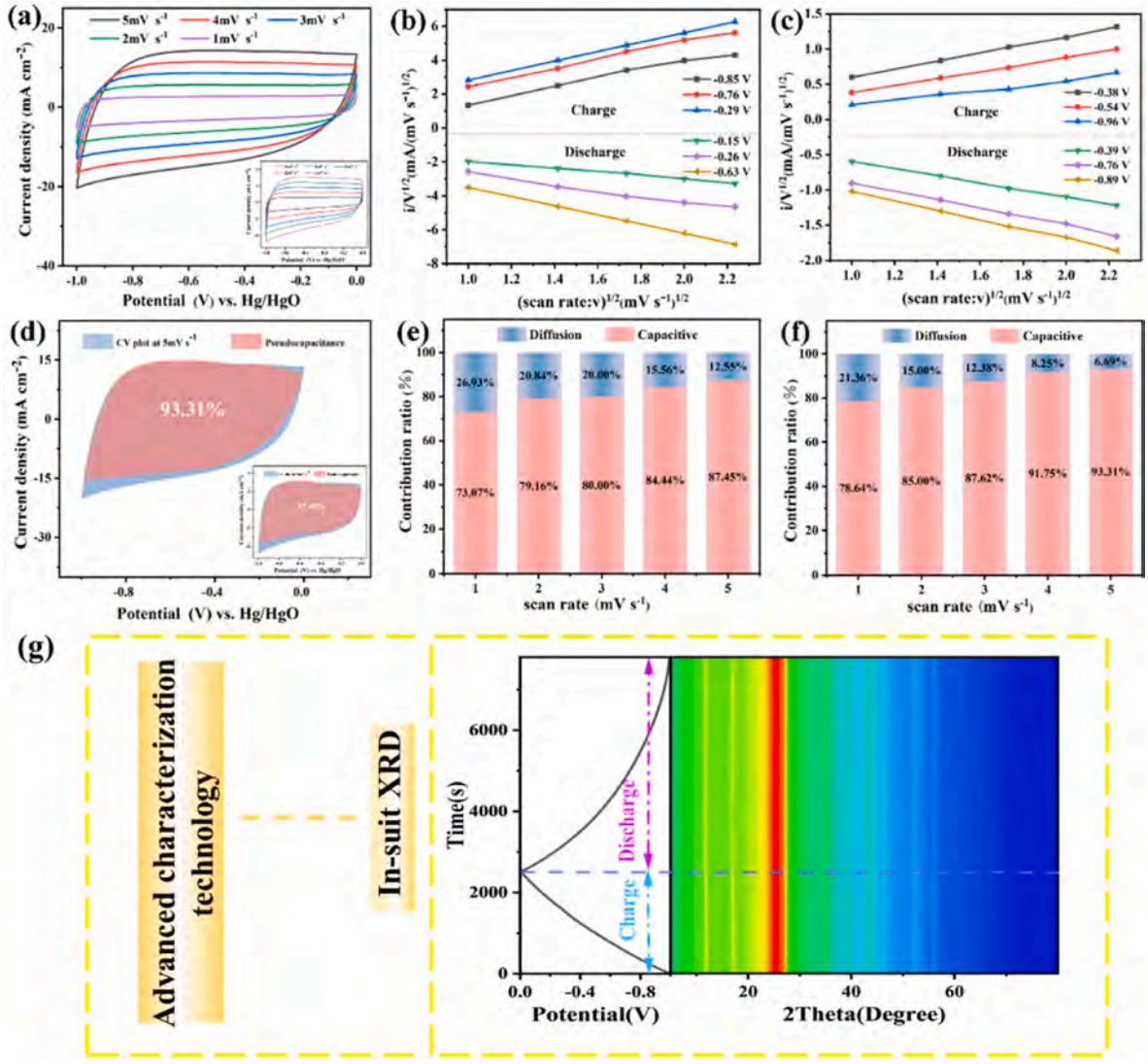

Fig. 5. (a) CV curves of FCO/Au/CPCN@CC, inset for FCO/CPCN@CC; (b,c) CV data of 6 groups of FCO/Au/CPCN@CC and (c) FCO/CPCN@CC at different voltages and k_1 calculated by equation (4); (d) Pseudocapacitance of the FCO/Au/CPCN@CC at 5 mV s^{-1} (inset for FCO/CPCN@CC); (e) Pseudocapacitance contribution ratios of FCO/CPCN@CC; (f) Pseudocapacitance contribution ratios of FCO/Au/CPCN@CC; (g) In-situ XRD of the FCO/Au/CPCN@CC.

capacitors are constructed. The composite material prepared served as the negative electrode, while activated carbon (AC) was utilized as the positive electrode. Two different electrolytes are used: a 1.0 M Na_2SO_4 solution in 2 V window (AC//FCO/Au/CPCN@CC-2V) for the aqueous supercapacitor and a 1.0 M $NaPF_6$ organic solution for the 4 V window (AC//FCO/Au/CPCN@CC-4V) for the organic system supercapacitor. Figs. S2(a)–S2(b) displays the electrochemical properties of the aqueous asymmetrical supercapacitor. AC//FCO/Au/CPCN@CC-2V exhibits a notably longer discharging time, accompanied by a greater CV area in comparison to the AC//FCO/CPCN@CC-2V. The CV and GCD curves of the AC electrode are shown in Fig. S12. Fig. 6(a) and (b) exhibit the electrochemical properties of organic system supercapacitors. At the same current density, the CV area of AC//FCO/Au/CPCN@CC-4V surpasses that of AC//FCO/CPCN@CC-4V. Specifically, at 1 mA cm^{-2}, the discharging duration of AC//FCO/Au/CPCN@CC-4V is approximately 31.2-fold compared to AC//FCO/CPCN@CC-4V. In different voltage windows, the GCD and CV data of AC//FCO/Au/CPCN@CC-2V (Figs. S2(c) and S2(d)) and AC//FCO/Au/CPCN@CC-4V (Fig. 6(c) and (d)) do not appear to be deformed. This indicates a good match between electrodes in the device, thereby broadening the work voltage. Fig. 6(e) and Fig. S3(a) display the CV data of AC//FCO/Au/CPCN@CC-2V together with AC//FCO/Au/CPCN@CC-4V under various scanning speeds. The curves show no distortion even when the scanning speed reaches 4800 mV s^{-1}, reflecting that the big area and swift ion diffusion result in the fast charging-discharging properties [57]. The GCD graphs of AC//FCO/Au/CPCN@CC-2V (Fig. S3(b)) and AC//FCO/Au/CPCN@CC-4V (Fig. 6(f)) at different current densities have a triangular shape indicative of favorable electrochemical properties, rapid I-V reaction, and high electrochemical reversibility. Fig. S4 presents the electrochemical test results of AC//FCO/CPCN@CC-4V, AC//FCO/Au/CPCN@CC-4V possesses a longer discharge duration and greater CV area.

Fig. 6(g) shows the analysis of EIS for supercapacitors, the AC//FCO/CPCN@CC configuration shows an electrolyte resistance (R_s) of 8.21Ω and a charge transfer resistance (R_{ct}) of 21.8Ω. In contrast, the AC//FCO/Au/CPCN@CC configuration has lower resistance values, with R_s at 6.69Ω and R_{ct} at 5.43Ω. As a result, the AC//FCO/Au/CPCN@CC demonstrates enhanced capacitance properties and enables faster electron and ion transfer during energy storage. The resistance values are summarized in Table S2. The stability of the SCs is tested through GCD. The retention rate of AC//FCO/Au/CPCN@CC-4V is 84.27 % following 10,000 cycles, surpassing that of AC//FCO/CPCN@CC-4V (61.39 %) without gold NPs. Additionally, the retention rate of AC//FCO/Au/CPCN@CC-2V is 84.52 % (Fig. S6(a)). These findings showcase the exceptional cycling capacity of the supercapacitor. Table S1 shows the

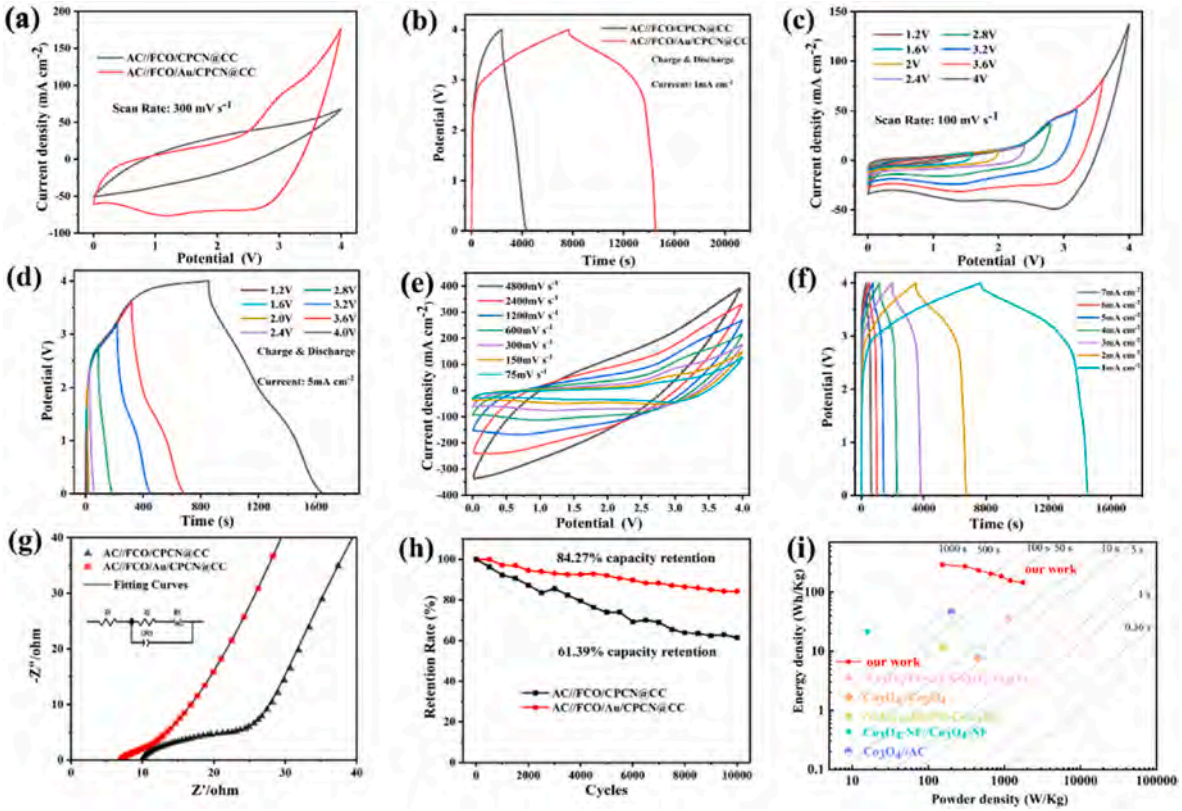

Fig. 6. (a) CV curves at 300 mV s^{-1} and (b) GCD curves at 1 mA cm^{-2} of AC//FCO/CPCN@CC-4V and AC//FCO/Au/CPCN-4V @CC; (c) GCD curves and (d) CV curves for different upper cut-off voltages; (e) CV curves at different scanning rates and (f) GCD curves at different current densities of AC//FCO/Au/CPCN@CC-4V; (g) Nyquist plots curves and (h) Long-term cycling performance of AC//FCO/CPCN@CC-4V and AC//FCO/Au/CPCN@CC-4V; (i) Ragone plots of the as-assembled ASC.

power densities, energy densities, as well as specific capacities of AC//FCO/Au/CPCN@CC-4V at diverse current densities calculated by formulas (1-3). AC//FCO/CPCN@CC-4V displays a maximum specific capacitance of 131.18 F g^{-1} and a peak energy density reaches 291.5 W h kg^{-1} when the power density reaches 153.85 W kg^{-1}, also at 1749.9 W kg^{-1}, its energy density maintains at 144.78 W h kg^{-1} with a capacitance of 65.15 F g^{-1}. Fig. 6(i) illustrates the Ragone plot of AC//FCO/Au/CPCN@CC-4V. The device delivers better electrochemical performance compared to previously documented devices, for example, Co_3O_4/Fe_2O_3//Co_3O_4/Fe_2O_3 (35.15 W h kg^{-1} at 1125 W kg^{-1}) [58], Co_3O_4//Co_3O_4 (7.9 W h kg^{-1} at 450 W kg^{-1}) [49], Ni-Co oxide//Ni-Co oxide (11.5 W h kg^{-1} at 158 W kg^{-1}) [59], Co_3O_4-NF//Co_3O_4-NF (21.5 W h kg^{-1} at 15.8 W kg^{-1}) [54], Co_3O_4//AC (44.99 W h kg^{-1} at 200 W kg^{-1}) [60]. Fig. S5 shows the capacitances of AC//FCO/Au/CPCN@CC-2V, which reaches 300 F g^{-1} at 1 mA cm^{-2}. Fig. S6 (b) depicts the Ragone plots of AC//FCO/Au/CPCN@CC-2V. The maximum energy density of this equipment is 166.67 W h kg^{-1}, the maximum power density is 233.81 W kg^{-1}, its performance surpasses that of CuO//Fe_2O_3 (23 W h kg^{-1} at 1900 W kg^{-1}) [61], $FeCo_2O_4$//GO (14.5 W h kg^{-1} at 2177 W kg^{-1}) [62], α-MnO_2@CNTs/CC//-Fe_2O_3@CNTs/CC (14.5 W h kg^{-1} at 2177 W kg^{-1}) [16], Co_3O_4-n//AC (15.5 W h kg^{-1} at 658 W kg^{-1}) [63], and Co_3O_4/CdO//AC (39.4 W h kg^{-1} at 864.35 W kg^{-1}) [64]. The findings indicate that flexible SCs with rapid charging capabilities and a broad voltage window exhibit significant potential for practical applications.

3.4. FCO-based sodium-ion batteries

The unique structure of FCO/Au/CPCN@CC enables a large power density and stability in supercapacitors. Hence, to comprehensively investigate the applicability of MOF-derived electrodes in battery technology and delineate the performance disparities in supercapacitors, a systematic study is performed within the domain of SIBs. Fig. 7(a) presents the cycling capabilities under 0.1C. The discharge capacity of the FCO/Au/CPCN@CC is 950 mAh g^{-1} after 50 cycles, surpassing that of the FCO/CPCN@CC (648 mAh g^{-1}) electrode. Fig. 7 (b) displays the rate performance of FCO/Au/CPCN@CC in SIBs. The reversible capacities of FCO/Au/CPCN@CC are recorded at 958, 876, 758, 480, 322, and 260 mAh g^{-1} under 0.1, 0.2, 0.3, 1, 2, and 3 C, respectively. Upon reverting to 0.1C, the capacity is restored to its initial value, demonstrating outstanding. In contrast, the FCO/CPCN@CC electrode has smaller discharge capacities of 676, 595, 466, 270,169, and 112 mAh g^{-1} at 0.1, 0.2, 0.3, 1, 2 and 3 C, respectively. These values are worse than those of the FCO/Au/CPCN@CC electrode, demonstrating that incorporating Au nanoparticles substantially enhances electrochemical performance.

To elucidate the redox reaction of the FCO/Au/CPCN@CC-based SIBs, CV data for the first three laps are attained from the sodium ion batteries (SIBs) at 0.1 mV s^{-1}, as shown in Fig. 7(c). The cathodic peaks occurring at 0.2 V have a relationship with the restoration of Fe_3O_4 and Co_3O_4 to Fe and Co in the first cycle. This reaction, indicative of the Solid Electrolyte Interphase (SEI) layer formation, is irreversible and the peak vanishes in subsequent cycles [65]. Two distinct cathode peaks subsequently emerge at 0.38 V and 1.45 V due to the conversion of Fe_3O_4 and Co_3O_4 to Fe and Co [66,67]. These findings are in close concordance with the voltage plateau in GCD curves (Fig. 7(d)). The anodic peaks at 0.45 as well as 1.5 V being consistent across the first and subsequent cycles indicate reversible oxidation of Fe and Co to Fe_3O_4 and Co_3O_4 during charging [68,69]. The alignment of the second and third CV curves suggests that the constructed battery exhibits excellent stability and cycling performance [70,71]. The CV profiles and GCD curves of the SIB utilizing an FCO/CPCN@CC electrode, performed at a scanning rate

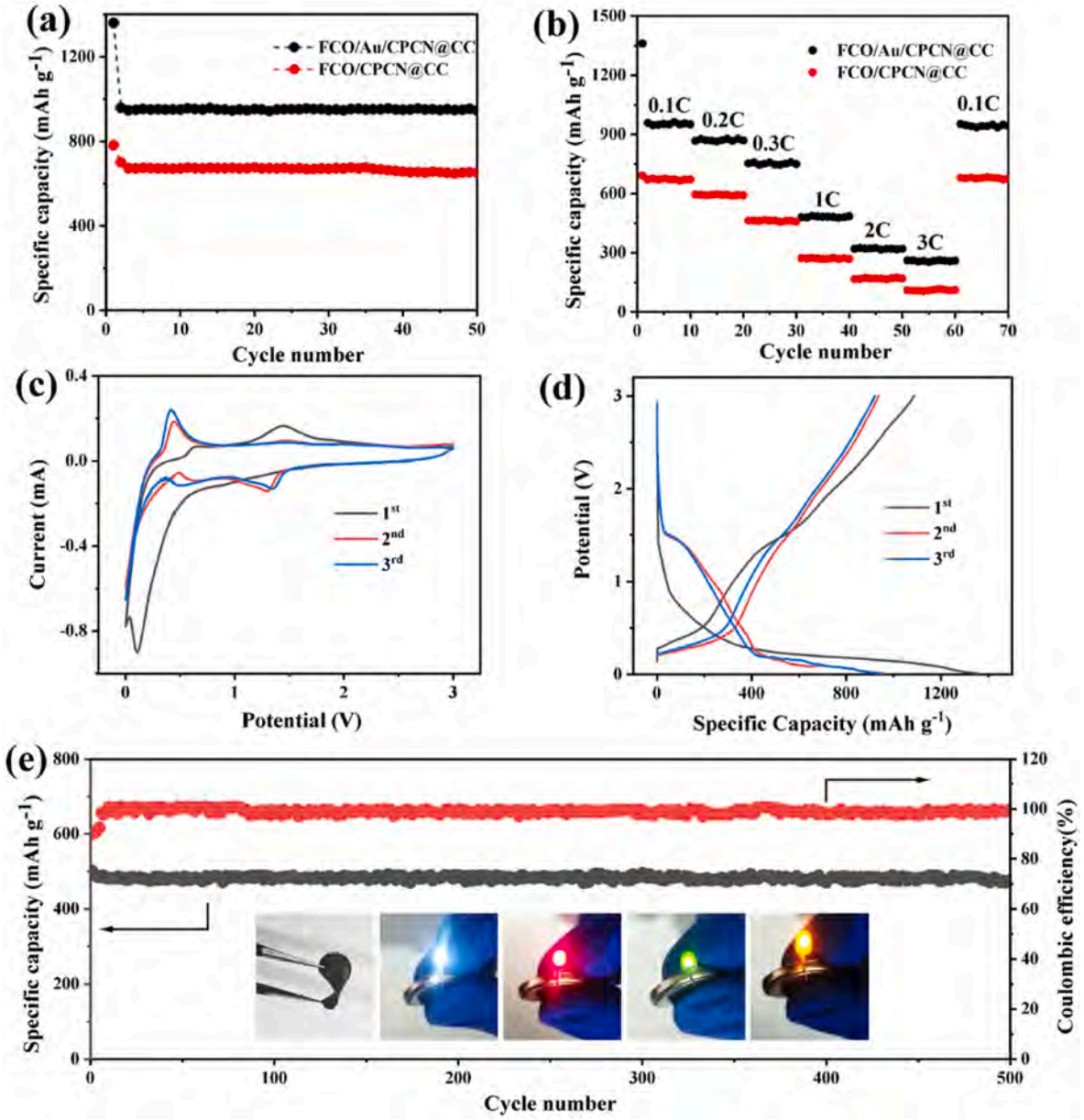

Fig. 7. (a) Cycling performance of FCO/CPCN@CC and FCO/Au/CPCN@CC for 50 cycles at 0.1C; (b) Rate performance of FCO/CPCN@CC and FCO/Au/CPCN@CC at various current densities; (c) CV curves and (d) GCD profiles of the FCO/Au/CPCN@CC; (e) Long-term cycling performance at 1 C.

of 0.1 mV s^{-1} and a current density of 0.1C, respectively, are presented in Figs. S14(a) and (b). Furthermore, the initial Coulombic efficiency stands at 70.5 %, with the irreversible capacity loss predominantly growing out of the development of the solid electrolyte interface layer [72]. Fig. 7(e) illustrates the favorable cycle stability of SIBs. At 1C, exhibiting a capacity of 480 mAh g^{-1} throughout 500 cycles, and the coulomb efficiency remains above 98 %. Furthermore, the sodium-ion battery (SIB) can easily power white, red, yellow, and green light-emitting diodes (LEDs). In the EIS analysis of sodium ion batteries (Fig. S14(c)), the resistance (R_s) for the FCO/Au/CPCN@CC electrode is measured at 8.52Ω, while the FCO/CPCN@CC electrode shows a higher R_s of 9.7Ω. Additionally, the FCO/Au/CPCN@CC electrode exhibits a lower charge transfer impedance (R_{ct}) of 17.59Ω, compared to the bimetallic FCO/CPCN@CC electrode, which has an R_{ct} of 26.65Ω. These results indicate that the FCO/Au/CPCN@CC electrode facilitates more efficient charge transfer, enhancing the overall performance of the sodium ion battery. The CV and GCD plots of FCO/Au/CPCN@CC based SIB at different scan rates and current densities are shown in Fig.S14 (d) and (e).

The adsorption energy and density of state are investigated by Density Functional Theory (DFT) calculation. The electrode's sodium ion adsorption model is depicted in Fig. 8(a)–(d). The calculated adsorption energies in Fig. 8(e) are negative, indicating that the process is exothermic. The FCO/Au/CPCN@CC electrode has lower adsorption energy, a stronger adsorption effect, and a more stable structure. Fig. 8 (f) and (g) illustrate the projected density of states (PDOS) for FCO/CPCN@CC and FCO/Au/CPCN@CC, respectively. Fig. 8(h) represents the density of states (DOS) diagram. Fe 3*d*, Co 4*d*, O 2*p*, and C 2*p* primarily influenced the electronic numbers near the Fermi level. In the FCO/Au/CPCN@CC electrode, the Au 5*d* orbitals show obvious peaks at −0.37 eV, −1.15 eV, and −2.3 eV, while the Fe 3*d*, Co 3*d*, Au 5*d*, and O 2*p* orbitals cross the Fermi level. Compared with FCO/CPCN@CC, FCO/Au/CPCN@CC exhibits metallic properties due to the gold particles. Furthermore, it has a greater concentration of electrons close to the Fermi level thus giving rise to superior conductivity. These characteristics enhance electron transfer and facilitate rapid reaction kinetics.

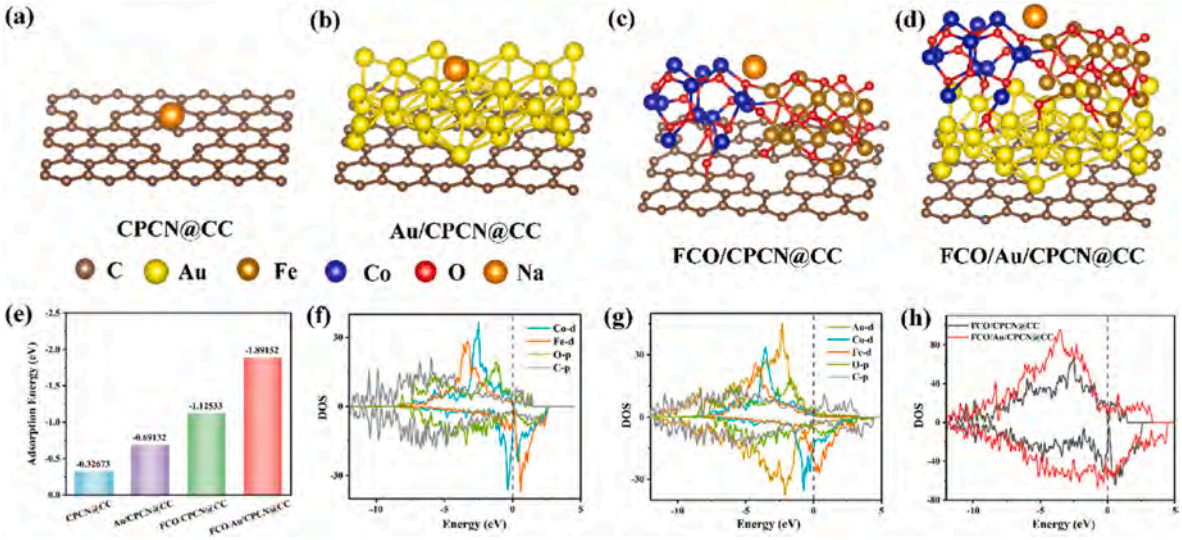

Fig. 8. (a–d) Adsorption model and (e) Adsorption energy of CPCN@CC, Au/CPCN@CC, FCO/CPCN@CC, and FCO/Au/CPCN@CC; (f, g) PDOS and (h) DOS of FCO/CPCN@CC, and FCO/Au/CPCN@CC.

4. Conclusion

The FCO/Au/CPCN@CC composite materials were fabricated through a hydrothermal process. The iron-cobalt oxide nanowires are intricately anchored on the gold-modified CPCN derived from the bimetallic MOFs. A three-electrode configuration was evaluated in a 1M Na_2SO_4 solution. SCs constructed utilizing a 1M $NaPF_6$ solution exhibit outstanding electrochemical performance within a 4V voltage range. The FCO/Au/CPCN@CC electrode shows a stable CV profile at 4800 mV s^{-1}, together with a peak energy density of 1090.8 W h kg^{-1} at 571.43 W kg^{-1} as well as an energy density of 344.89 W h kg^{-1} at the maximum power density of 4000 W kg^{-1}. Upon 10,000 cycles of GCD, the ratio of capacitance stands at 84.27 %. FCO/Au/CPCN@CC can also play the part of efficient anode materials for SIBs, possessing high-speed capabilities and outstanding cyclic endurance. At 0.1C, the discharging capacity reaches 958 mAh g^{-1} and nearly regains its original value after cycling. Following 500 cycles at 1C, the Coulombic efficiency outstrips 98 %, and the discharge capacity maintains at 480 mAh g^{-1}. The results reveal the dual functionalities of FCO/Au/CPCN@CC in both supercapacitors and SIBs and highlight the immense potential in energy storage devices.

CRediT authorship contribution statement

Hanxue Zhao: Writing – original draft, Methodology, Investigation, Formal analysis, Data curation. **Wendong Xu:** Methodology, Investigation, Formal analysis, Data curation, Conceptualization. **Mai Li:** Writing – review & editing, Validation, Supervision, Resources, Project administration. **Zheyi Meng:** Software, Resources, Conceptualization. **Inaam Ullah:** Visualization, Investigation. **Muhammad Zubair Nawaz:** Software, Conceptualization. **Jiale Wang:** Investigation. **Chunrui Wang:** Investigation. **Paul K. Chu:** Resources.

Declaration of competing interest

We have no competing interests, including but not limited to employment, consultancy, patents, honoraria, or ownership of stocks or shares in any organization that may influence our research in any way.

Acknowledgments

The study was financially sponsored by the Fundamental Research Funds for the Central Universities (No. 2232024D-31), National Natural Science Foundation of China (No. 22005046), City University of Hong Kong Donation Research Grants (DON-RMG 9229021 and 9220061), and City University of Hong Kong Strategic Research Grant (SRG) (No. 7005105).

Appendix A. Supplementary data

Supplementary data to this article can be found online at https://doi.org/10.1016/j.jpowsour.2024.235793.

Data availability

Data will be made available on request.

References

[1] Z. Pan, S. Yu, L. Wang, C. Li, F. Meng, N. Wang, S. Zhou, Y. Xiong, Z. Wang, Y. Wu, X. Liu, B. Fang, Y. Zhang, Recent advances in porous carbon materials as electrodes for supercapacitors, Nanomaterials 13 (2023) 1744, https://doi.org/10.3390/nano13111744.

[2] Z. Zhai, L. Zhang, T. Du, B. Ren, Y. Xu, S. Wang, J. Miao, Z. Liu, A review of carbon materials for supercapacitors, Mater. Des. 221 (2022) 111017, https://doi.org/10.1016/j.matdes.2022.111017.

[3] A.E.-S. Etman, A.M. Ibrahim, F.A.-Z.M. Darwish, K.F. Qasim, A 10 years-developmental study on conducting polymers composites for supercapacitors electrodes: a review for extensive data interpretation, J. Ind. Eng. Chem 122 (2023) 27–45, https://doi.org/10.1016/j.jiec.2023.03.008.

[4] A.S. Mohammed, S.M. Atnaw, A.O. Salau, J.N. Eneh, Review of optimal sizing and power management strategies for fuel cell/battery/supercapacitor hybrid electric vehicles, Energy Rep. 9 (2023) 2213–2228, https://doi.org/10.1016/j.egyr.2023.01.042.

[5] N. Nhat-An, V. Hien, M. Pedram, D. Shin, An attachable battery-supercapacitor hybrid for large pulsed load, IEEE Des Test 39 (2022) 62–69, https://doi.org/10.1109/mdat.2022.3177709.

[6] M.Z. Iqbal, M.M. Faisal, S.R. Ali, M. Alzaid, A facile approach to investigate the charge storage mechanism of MOF/PANI based supercapattery devices, Solid State Ion 354 (2020) 115411, https://doi.org/10.1016/j.ssi.2020.115411.

[7] B. Babu, J. Kim, K. Yoo, Nanocomposite of SnO_2 quantum dots and Au nanoparticles as a battery-like supercapacitor electrode material, ACS Mater. Lett. 309 (2022) 131339, https://doi.org/10.1016/j.matlet.2021.131339.

[8] K. Roy, T. Li, S. Ogale, N. Robertson, Hybrid perovskite-like iodobismuthates as low-cost and stable anode materials for lithium-ion battery applications, J. Mater. Chem. A 9 (2021) 2689–2693, https://doi.org/10.1039/d0ta07414d.

[9] W. Dong, M. Xie, S. Zhao, Q. Qin, F. Huang, Materials design and preparation for high energy density and high power density electrochemical supercapacitors, Mat. Sci. Eng. R 152 (2023) 100713, https://doi.org/10.1016/j.mser.2022.100713.

[10] J. Huang, Y. Xie, Y. You, J. Yuan, Q. Xu, H. Xie, Y. Chen, Rational design of electrode materials for advanced supercapacitors: from lab research to commercialization, Adv. Funct. 33 (2023) 2213095, https://doi.org/10.1002/adfm.202213095.

[11] L. Pang, H. Wang, Inorganic aqueous anionic redox liquid electrolyte for supercapacitors, Adv. Mater. Technol. 7 (2021) 2100501, https://doi.org/10.1002/admt.202100501.

[12] Y. Dai, C. Liu, Y. Bai, Q. Kong, H. Pang, Framework materials for supercapacitors, Nanotechnol 11 (2022) 1005–1046, https://doi.org/10.1515/ntrev-2022-0042.

[13] D. Tian, Y. Ao, W. Li, J. Xu, C. Wang, General fabrication of metal-organic frameworks on electrospun modified carbon nanofibers for high-performance asymmetric supercapacitors, J. Colloid Interface Sci. 603 (2021) 199–209, https://doi.org/10.1016/j.jcis.2021.05.138.

[14] F. Yang, K. Xu, J. Hu, Construction of Co_3O_4@Fe_2O_3 core-shell nanowire arrays electrode for supercapacitors, J. Alloys Compd. 729 (2017) 1172–1176, https://doi.org/10.1016/j.jallcom.2017.09.259.

[15] V. Molahalli, C. K, M.K. Singh, M. Agrawal, S.G. Krishnan, G. Hegde, Past decade of supercapacitor research - lessons learned for future innovations, J. Energy Storage 70 (2023) 108062, https://doi.org/10.1016/j.est.2023.108062.

[16] M. Li, K.L. Zhu, H.X. Zhao, Z.Y. Meng, C.R. Wang, P.K. Chu, Construction of alpha-MnO_2 on carbon fibers modified with carbon nanotubes for ultrafast flexible supercapacitors in ionic liquid electrolytes with wide voltage windows, Nanomaterials 12 (2022) 2020, https://doi.org/10.3390/nano12122020.

[17] J. Wei, L. Zhong, H. Xia, Z. Lv, C. Diao, W. Zhang, X. Li, Y. Du, S. Xi, M. Salanne, X. Chen, S. Li, Metal-ion oligomerization inside electrified carbon micropores and its effect on capacitive charge storage, Adv. Mater. 34 (2021) 2107439, https://doi.org/10.1002/adma.202107439.

[18] Y.A. Kumar, G. Koyyada, T. Ramachandran, J.H. Kim, S. Sajid, M. Moniruzzaman, S. Alzahmi, I.M. Obaidat, Carbon materials as a conductive skeleton for supercapacitor electrode applications: a review, Nanomaterials 13 (2023) 1049, https://doi.org/10.3390/nano13061049.

[19] W. Wang, J. Cao, J.W. Yu, F.J. Tian, X.Y. Luo, Y.T. Hao, J.Y. Huang, F.C. Wang, W. Q. Zhou, J.K. Xu, X.M. Liu, H.J. Yang, Flexible supercapacitors based on stretchable conducting polymer electrodes, Polymers 15 (2023) 1856, https://doi.org/10.3390/polym15081856.

[20] W.L. Luo, Y. Ma, T.X. Li, H.K. Thabet, C.P. Hou, M.M. Ibrahim, S.M. El-Bahy, B. B. Xu, Z.H. Guo, Overview of MXene/conducting polymer composites for supercapacitors, J. Energy Storage 52 (2022) 105008, https://doi.org/10.1016/j.est.2022.105008.

[21] A. Pramitha, Y. Raviprakash, Recent developments and viable approaches for high-performance supercapacitors using transition metal-based electrode materials, J. Energy Storage 49 (2022) 104120, https://doi.org/10.1016/j.est.2022.104120.

[22] X. Lu, T. Zhai, X. Zhang, Y. Shen, L. Yuan, B. Hu, L. Gong, J. Chen, Y. Gao, J. Zhou, Y. Tong, Z.L. Wang, WO_{3-x}@Au@MnO_2 core-shell nanowires on carbon fabric for high-performance flexible supercapacitors, Adv. Mater. 24 (2012) 938–944, https://doi.org/10.1002/adma.201104113.

[23] Y. Wang, J. Zhou, Z. Zhou, H. Lv, B. Gu, K. Wang, Z. Chen, X. Yan, J. Zhang, W.-W. Liu, Y.-L. Chueh, In situ synthesis of Fe_2O_3 nanosphere/Co_3O_4 nanowire-connected reduced graphene oxide hybrid networks for high-performance supercapacitors, Nanoscale 13 (2021) 15431–15444, https://doi.org/10.1039/d1nr00126d.

[24] X. Yang, X. Sun, L.-Y. Gan, L. Sun, H. Mi, P. Zhang, X. Ren, Y. Li, A CoO_x/FeO_x heterojunction on carbon nanotubes prepared by plasma-enhanced atomic layer deposition for the highly efficient electrocatalysis of oxygen evolution reactions, J. Mater. Chem. A 8 (2020) 15140–15147, https://doi.org/10.1039/c9ta13492a.

[25] X. Cao, J. He, H. Li, L. Kang, X. He, J. Sun, R. Jiang, H. Xu, Z. Lei, Z.-H. Liu, $CoNi_2S_4$ nanoparticle/carbon nanotube sponge cathode with ultrahigh capacitance for highly compressible asymmetric supercapacitor, Small 14 (2018) 1800998, https://doi.org/10.1002/smll.201800998.

[26] D. Chen, S. Zhou, H. Quan, R. Zou, W. Gao, X. Luo, L. Guo, Tetsubo-like α-Fe_2O_3/C nanoarrays on carbon cloth as negative electrode for high-performance asymmetric supercapacitors, Chem. Eng. J. 341 (2018) 102–111, https://doi.org/10.1016/j.cej.2018.02.021.

[27] H. Gong, S. Bie, J. Zhang, X. Ke, X. Wang, J. Liang, N. Wu, Q. Zhang, C. Luo, Y. Jia, In situ construction of ZIF-67-derived hybrid tricobalt Tetraoxide@Carbon for supercapacitor, Nanomaterials 12 (2022) 1571, https://doi.org/10.3390/nano12091571.

[28] J. Meng, Z. Cui, X. Yang, S. Zhu, Z. Li, K. Qi, L. Zheng, Y. Liang, Cobalt-iron (oxides) water oxidation catalysts: tracking catalyst redox states and reaction dynamic mechanism, J. Catal. 365 (2018) 227–237, https://doi.org/10.1016/j.jcat.2018.06.031.

[29] J. Su, S. Liu, J. Wang, C. Liu, Y. Li, D. Wu, Solution-based synthesis of carbon-hematite composite thin films for high-performance supercapacitor applications, MRS Commun 6 (2016) 367–374, https://doi.org/10.1557/mrc.2016.60.

[30] Y. Li, X. Han, T. Yi, Y. He, X. Li, Review and prospect of $NiCo_2O_4$-based composite materials for supercapacitor electrodes, J. Energy Chem. 31 (2019) 54–78, https://doi.org/10.1016/j.jechem.2018.05.010.

[31] H. Zhang, X. Lu, L. Yang, Y. Hu, M. Yuan, C. Wang, Q. Liu, F. Yue, D. Zhou, Q. Xia, Efficient air epoxidation of cycloalkenes over bimetal-organic framework ZnCo-MOF materials, Mol. Catal. 499 (2021) 111300, https://doi.org/10.1016/j.mcat.2020.111300.

[32] X.W. Wang, K.P. Cai, M.R. Manikandan, P.A. Lu, P.F. Yang, M.Y. Shang, H.R. Song, W.L. Zhao, Y.X. Fu, J. Liu, W.B. Lou, R.Y. Zhang, Y.C. Hu, J. Shang, S.Q. Yin, Facile synthesis of nickel-based bimetallic metalorganic frameworks with different cobalt ratios as electrode material for electrochemical supercapacitors, Appl. Phys. 128 (2022) 953, https://doi.org/10.1007/s00339-022-06095-7.

[33] Y.N. Liang, W.G. Yao, J.X. Duan, M. Chu, S.Z. Sun, X. Li, Nickel cobalt bimetallic metal-organic frameworks with a layer-and-channel structure for high-performance supercapacitors, J. Energy Storage 33 (2021) 102149, https://doi.org/10.1016/j.est.2020.102149.

[34] G.J.H. Lim, X.M. Liu, C. Guan, J. Wang, Co/Zn bimetallic oxides derived from metal organic frameworks for high performance electrochemical energy storage, Electrochim 291 (2018) 177–187, https://doi.org/10.1016/j.electacta.2018.08.105.

[35] L. Chen, H.F. Wang, C. Li, Q. Xu, Bimetallic metal-organic frameworks and their derivatives, Chem. Sci. 11 (2020) 5369–5403, https://doi.org/10.1039/d0sc01432j.

[36] S. Dang, Q.-L. Zhu, Q. Xu, Nanomaterials derived from metal–organic frameworks, Nat. Rev. Mater. 3 (2017) 17075, https://doi.org/10.1038/natrevmats.2017.75.

[37] J.-K. Sun, Q. Xu, Functional materials derived from open framework templates/precursors: synthesis and applications, Energy Environ. 7 (2014) 2071–2100, https://doi.org/10.1039/c4ee00517a.

[38] N.L. Torad, R.R. Salunkhe, Y. Li, H. Hamoudi, M. Imura, Y. Sakka, C.C. Hu, Y. Yamauchi, Electric double-layer capacitors based on highly graphitized nanoporous carbons derived from ZIF-67, Chem. Eur J. 20 (2014) 7895–7900, https://doi.org/10.1002/chem.201400089.

[39] D. He, Y. Gao, Y. Yao, L. Wu, J. Zhang, Z.H. Huang, M.X. Wang, Asymmetric supercapacitors based on hierarchically nanoporous carbon and $ZnCo_2O_4$ from a single biometallic metal-organic frameworks (Zn/Co-MOF), Front. Times 8 (2020) 719, https://doi.org/10.3389/fchem.2020.00719.

[40] K. Zhang, H. Hu, W. Yao, C. Ye, Flexible and all-solid-state supercapacitors with long-time stability constructed on PET/Au/polyaniline hybrid electrodes, J. Mater. Chem. A 3 (2015) 617–623, https://doi.org/10.1039/c4ta05605a.

[41] S. Anshu, S. Priya, D. Mandal, R. Rahul, T. Singh, A. Chandra, 2D flakes of Au decorated SnO_2 nanoparticles as electrode material for high performing supercapacitor, J. Phys. D 56 (2023) 205501, https://doi.org/10.1088/1361-6463/acc33f.

[42] M. Li, Z.Y. Meng, R.C. Feng, K.L. Zhu, F.F. Zhao, C.R. Wang, J.L. Wang, L.W. Wang, P.K. Chu, Fabrication of bimetallic oxides (MCo_2O_4: M=Cu, Mn) on ordered microchannel electro-conductive plate for high-performance hybrid supercapacitors, Sustainbility 13 (2021) 9896, https://doi.org/10.3390/su13179896.

[43] G. Kresse, J. Furthmuller, Efficiency of ab-initio total energy calculations for metals and semiconductors using a plane-wave basis set, Comput. Times 6 (1996) 15–50, https://doi.org/10.1016/0927-0256(96)00008-0.

[44] G. Kresse, J. Furthmuller, Efficient iterative schemes for ab initio total-energy calculations using a plane-wave basis set, Phys. Rev. B 54 (1996) 11169–11186, https://doi.org/10.1103/PhysRevB.54.11169.

[45] J.P. Perdew, K. Burke, M. Ernzerhof, Generalized gradient approximation made simple, Phys. Rev. Lett. 77 (1996) 3865–3868, https://doi.org/10.1103/PhysRevLett.77.3865.

[46] G. Kresse, D. Joubert, From ultrasoft pseudopotentials to the projector augmented-wave method, Phys. Rev. B 59 (1999) 1758–1775, https://doi.org/10.1103/PhysRevB.59.1758.

[47] P.E. Blochl, Projector augmented-wave method, Phys. Rev. B 50 (1994) 17953–17979, https://doi.org/10.1103/PhysRevB.50.17953.

[48] S. Grimme, J. Antony, S. Ehrlich, H. Krieg, A consistent and accurate ab initio parametrization of density functional dispersion correction (DFT-D) for the 94 elements H-Pu, Chem. Phys. 132 (2010) 154104, https://doi.org/10.1063/1.3382344.

[49] A.K. Singh, D. Sarkar, Substrate-integrated core–shell Co_3O_4@Au@CuO hybrid nanowires as efficient cathode materials for high-performance asymmetric supercapacitors with excellent cycle life, J. Mater. Chem. A 5 (2017) 21715–21725, https://doi.org/10.1039/c7ta07266j.

[50] R.R. Salunkhe, J. Tang, Y. Kamachi, T. Nakato, J.H. Kim, Y. Yamauchi, Asymmetric supercapacitors using 3D nanoporous carbon and cobalt oxide electrodes synthesized from a single metal-organic framework, ACS Nano 9 (2015) 6288–6296, https://doi.org/10.1021/acsnano.5b01790.

[51] M. Harilal, B. Vidyadharan, I.I. Misnon, G.M. Anilkumar, A. Lowe, J. Ismail, M. M. Yusoff, R. Jose, One-dimensional assembly of conductive and capacitive metal oxide electrodes for high-performance asymmetric supercapacitors, ACS Appl. Mater. 9 (2017) 10730–10742, https://doi.org/10.1021/acsami.7b00676.

[52] Y. Li, J. Xu, T. Feng, Q. Yao, J. Xie, H. Xia, Fe_2O_3 nanoneedles on ultrafine nickel nanotube arrays as efficient anode for high-performance asymmetric supercapacitors, Adv. Funct. Mater. 27 (2017) 1606728, https://doi.org/10.1002/adfm.201606728.

[53] X. Yang, H. Sun, L. Zhang, L. Zhao, J. Lian, Q. Jiang, High efficient photo-fenton catalyst of α-Fe_2O_3/MoS_2 hierarchical nanoheterostructures: reutilization for supercapacitors, Sci. Rep. 6 (2016) 31591, https://doi.org/10.1038/srep31591.

[54] C. Guan, W. Zhao, Y. Hu, Z. Lai, X. Li, S. Sun, H. Zhang, A.K. Cheetham, J. Wang, Cobalt oxide and N-doped carbon nanosheets derived from a single two-dimensional metal-organic framework precursor and their application in flexible asymmetric supercapacitors, Nanoscale Horiz 2 (2017) 99–105, https://doi.org/10.1039/c6nh00224b.

[55] N.R. Chodankar, D.P. Dubal, Y. Kwon, D.-H. Kim, Direct growth of $FeCo_2O_4$ nanowire arrays on flexible stainless steel mesh for high-performance asymmetric supercapacitor, NPG Asia Mater. 9 (2017) e419, https://doi.org/10.1038/am.2017.145 e419.

[56] X. Deng, Z. Wei, C. Cui, Q. Liu, C. Wang, J. Ma, Oxygen-deficient anatase TiO_2@C nanospindles with pseudocapacitive contribution for enhancing lithium storage, J. Mater. Chem. A 6 (2018) 4013–4022, https://doi.org/10.1039/c7ta11301c.

[57] M. Li, K.L. Zhu, Z.Y. Meng, R.H. Hu, J.L. Wang, C.R. Wang, P.K. Chu, Efficient coupling of MnO_2/TiN on carbon cloth positive electrode and Fe_2O_3/TiN on carbon cloth negative electrode for flexible ultra-fast hybrid supercapacitors, RSC Adv. 11 (2021) 35726–35736, https://doi.org/10.1039/d1ra05742a.

[58] X. Wei, Y. Li, H. Peng, D. Gao, Y. Ou, Y. Yang, J. Hu, Y. Zhang, P. Xiao, A novel functional material of Co_3O_4/Fe_2O_3 nanocubes derived from a MOF precursor for high-performance electrochemical energy storage and conversion application, Chem. Eng. J 355 (2019) 336–340, https://doi.org/10.1016/j.cej.2018.08.009.
[59] X. Lu, X. Huang, S. Xie, T. Zhai, C. Wang, P. Zhang, M. Yu, W. Li, C. Liang, Y. Tong, Controllable synthesis of porous nickel–cobalt oxide nanosheets for supercapacitors, Chem. Mater. 22 (2012) 13357–13364, https://doi.org/10.1039/c2jm30927k.
[60] H. Chen, C. Xue, Z. Hai, D. Cui, M. Liu, Y. Li, W. Zhang, Facile synthesis of 3D gem shape Co_3O_4 with mesoporous structure as electrode for high-performance supercapacitors, J. Alloys Compd. 819 (2020) 152939, https://doi.org/10.1016/j.jallcom.2019.152939.
[61] A.V. Shinde, N.R. Chodankar, V.C. Lokhande, A.C. Lokhande, T. Ji, J.H. Kim, C. D. Lokhande, Highly energetic flexible all-solid-state asymmetric supercapacitor with Fe_2O_3 and CuO thin films, RSC Adv. 6 (2016) 58839–58843, https://doi.org/10.1039/c6ra11896h.
[62] F.I. Saaid, A. Arsyad, N.S.H. Azman, A. Kumar, C.-C. Yang, T.-Y. Tseng, T. Winie, The synergistic effect of iron cobaltite compare to its single oxides as cathode in supercapacitor, J. Electroceramics 44 (2020) 183–194, https://doi.org/10.1007/s10832-020-00209-4.
[63] J. Li, G. Zan, Q. Wu, An ultra-high-performance anode material for supercapacitors: self-assembled long Co_3O_4 hollow tube network with multiple heteroatom (C-, N- and S-) doping, J. Mater. Chem. A 4 (2016) 9097–9105, https://doi.org/10.1039/c6ta02376b.
[64] X. Wang, Y. Yang, F. Zhang, J. Tang, Z. Guo, Facile synthesis of Co_3O_4/CdO nanospheres as high rate performance supercapacitors, Mater. Lett. 261 (2020) 127141, https://doi.org/10.1016/j.matlet.2019.127141.
[65] L. Xiao, D. Wu, S. Han, Y. Huang, S. Li, M. He, F. Zhang, X. Feng, Self-assembled Fe_2O_3/graphene aerogel with high lithium storage performance, ACS Appl. Mater. 5 (2013) 3764–3769, https://doi.org/10.1021/am400387t.
[66] L. Zhang, H.B. Wu, S. Madhavi, H.H. Hng, X.W. Lou, Formation of Fe_2O_3 microboxes with hierarchical shell structures from metal-organic frameworks and their lithium storage properties, J. Am. Chem. Soc. 134 (2012) 17388–17391, https://doi.org/10.1021/ja307475c.
[67] Z. Yan, Q. Hu, G. Yan, H. Li, K. Shih, Z. Yang, X. Li, Z. Wang, J. Wang, Co_3O_4/Co nanoparticles enclosed graphitic carbon as anode material for high performance Li-ion batteries, Chem. Eng. J. 321 (2017) 495–501, https://doi.org/10.1016/j.cej.2017.03.146.
[68] F. Han, D. Li, W.-C. Li, C. Lei, Q. Sun, A.-H. Lu, Nanoengineered polypyrrole-coated Fe_2O_3@C multifunctional composites with an improved cycle stability as lithium-ion anodes, Adv. Funct. Mater. 23 (2013) 1692–1700, https://doi.org/10.1002/adfm.201202254.
[69] Y. Chai, X. Wang, Y. Yu, X. Shi, Q. Zhang, N. Wang, Cooperation of Fe_2O_3@C and Co_3O_4/C subunits enhances the cyclic stability of Fe_2O_3@C/Co_3O_4 electrodes for lithium-ion batteries, Int. J. Energy Res. 43 (2019) 6045–6055, https://doi.org/10.1002/er.4705.
[70] C. Yan, G. Chen, J. Sun, X. Zhou, C. Lv, A novel anode comprised of C&N co-doped Co_3O_4 hollow nanofibres with excellent performance for lithium-ion batteries, Phys. Chem. Chem. Phys. 18 (2016) 19531–19535, https://doi.org/10.1039/c6cp02660e.
[71] Y. Dou, J. Xu, B. Ruan, Q. Liu, Y. Pan, Z. Sun, S.X. Dou, Atomic layer-by-layer Co_3O_4/graphene composite for high performance lithium-ion batteries, Adv. Energy Mater. 6 (2016) 1501835, https://doi.org/10.1002/aenm.201501835.
[72] T. Li, A. Qin, L. Yang, J. Chen, Q. Wang, D. Zhang, H. Yang, In situ grown Fe_2O_3 single crystallites on reduced graphene oxide nanosheets as high performance conversion anode for sodium-ion batteries, ACS Appl. Mater. 9 (2017) 19900–19907, https://doi.org/10.1021/acsami.7b04407.

Supporting Information

(Fe, Co) oxide Nanowires on Gold Nanoparticles modified MOF-derived Carbon Nanoflakes for high-efficiency Sodium-ion Batteries and Supercapacitors Across Electrolytes

Hanxue Zhao[a,1], Wendong Xu[a,1], Mai Li[a*], Zheyi Meng[b], Inaam Ullah[a], Muhammad Zubair Nawaz[c], Jiale Wang[a], Chunrui Wang[a], Paul K. Chu[d]

[a] College of Science, Donghua University, Shanghai 201620, China

[b] State Key Laboratory for Modification of Chemical Fibers and Polymer Materials, College of Material Science, Donghua University, Shanghai 201620, China

[c] Southern University of Science and Technology, Shenzhen, China

[d] Department of Physics, Department of Materials Science and Engineering, and Department of Biomedical Engineering, City University of Hong Kong, Tat Chee Avenue, Kowloon, Hong Kong, China

* Corresponding author: E-mail: limai@dhu.edu.cn (M. Li)

[1] These authors contributed equally to this work

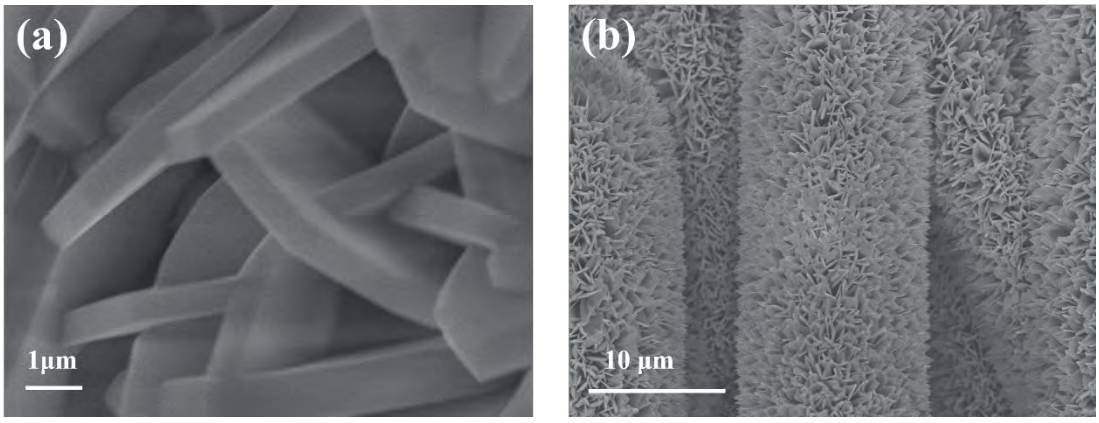

Fig. S1. (a, b) SEM images of ZnCo-MOF at different magnifications.

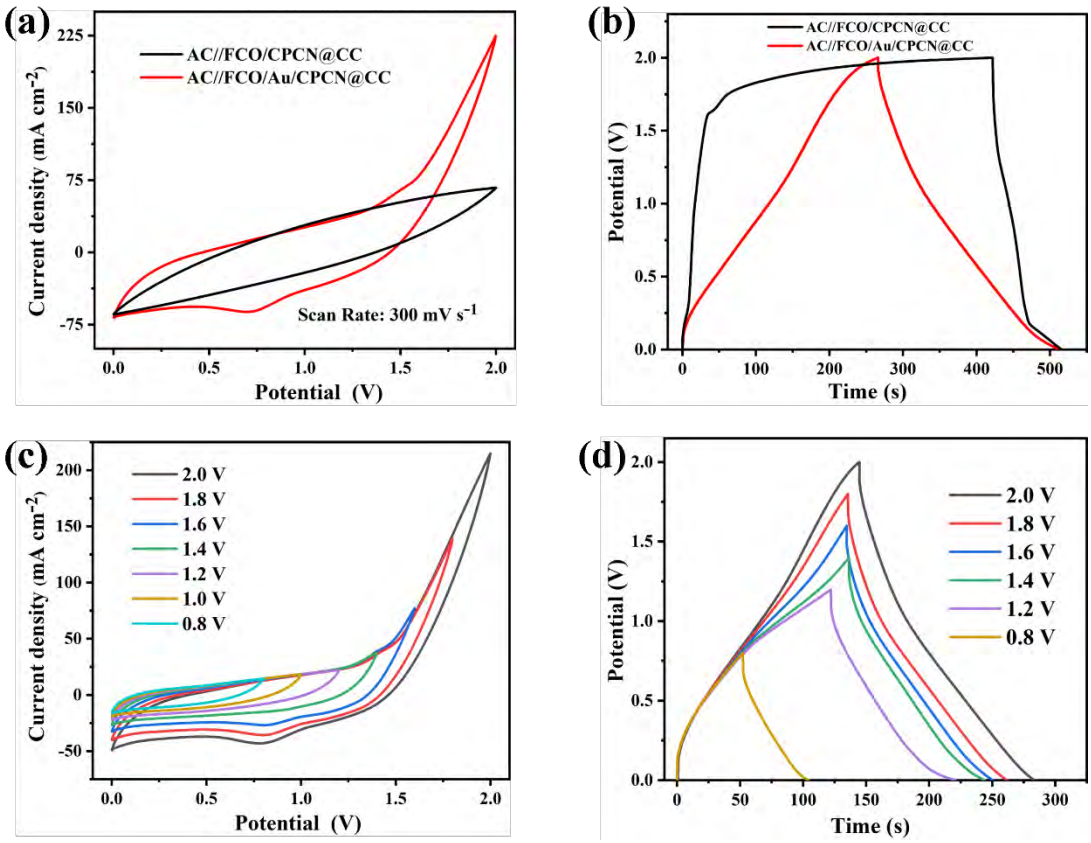

Fig. S2. (a) CV curves at 300 mV s^{-1} and (b) GCD curves at 4 mA cm^{-2} of AC// FCO/CPCN@-2V and AC// FCO/Au/CPCN@CC-2V; (c) CV curves and (d) GCD curves with different upper cut-off voltages of AC// FCO/Au/CPCN@CC-2V.

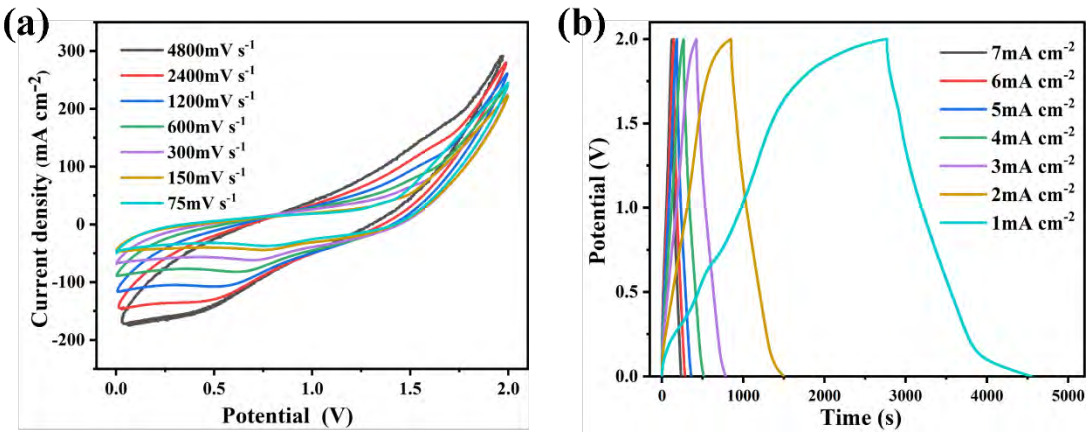

Fig. S3. (a) CV curves at different scanning rates and (b) GCD curves at different current densities of AC// FCO/Au/CPCN@CC-2V.

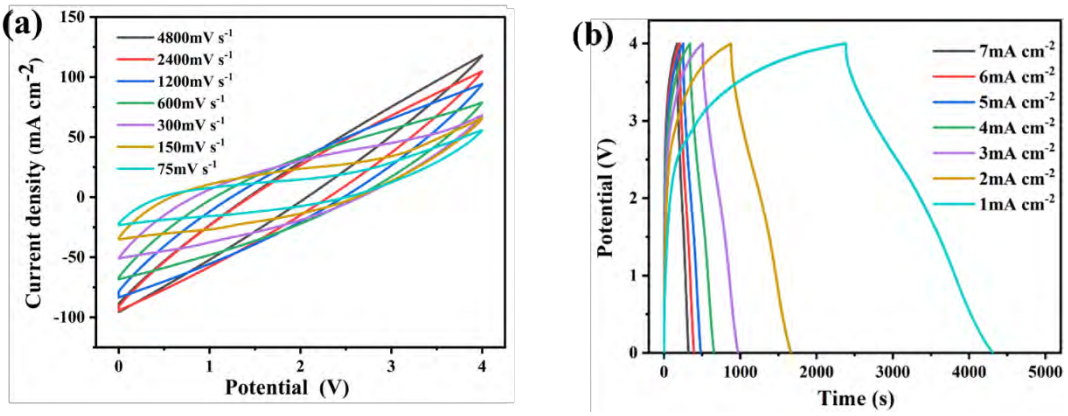

Fig. S4. (a) CV, (b) GCD curves of AC// FCO/CPCN@CC-4V.

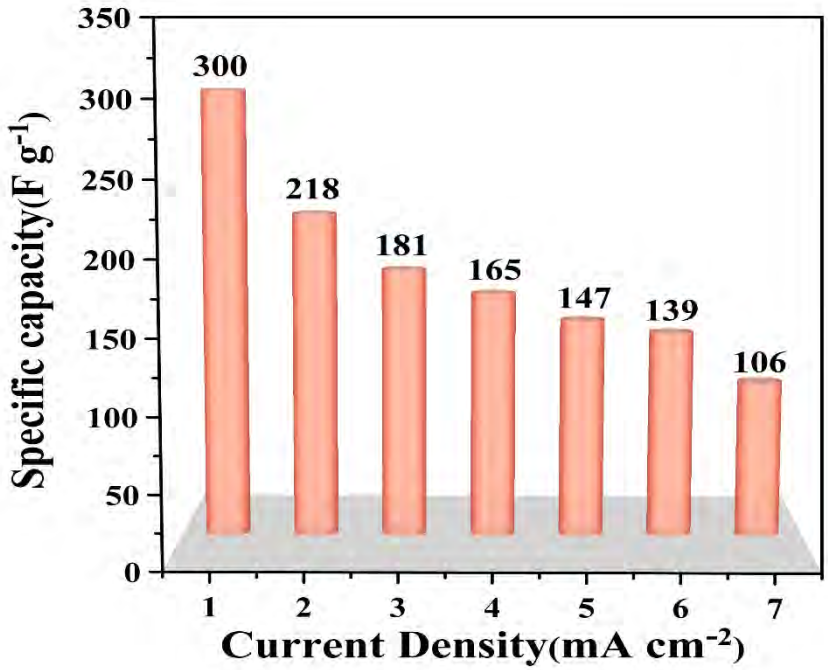

Fig. S5. Specific capacitance at different current densities of AC// FCO/Au/CPCN@CC-2V.

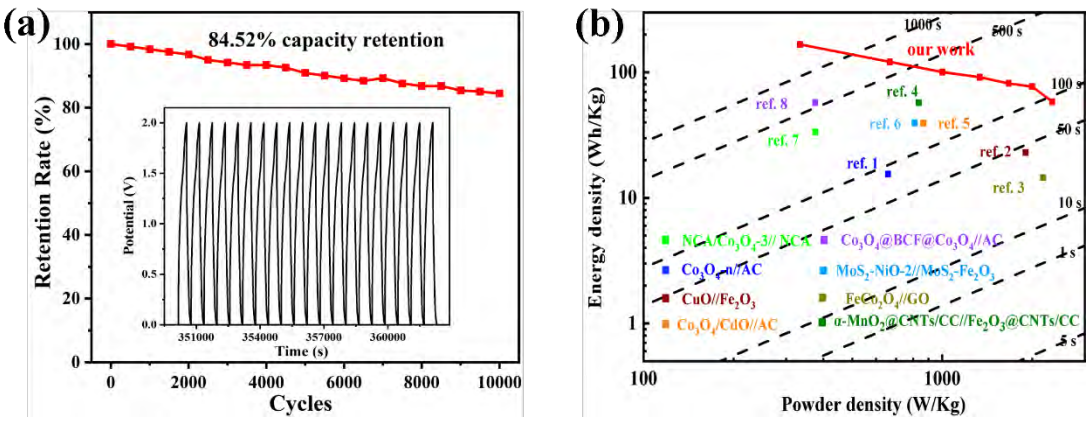

Fig. S6. (a) Long-term performance of AC// FCO/Au/CPCN@CC-2V; (b) Ragone plot of the as-assembled ASC.

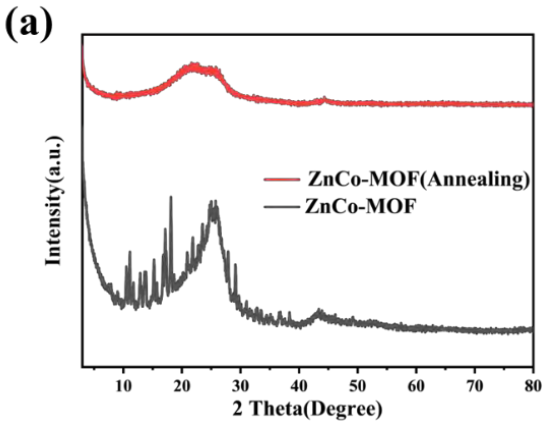

Fig. S7. (a) XRD spectra of ZnCo-MOF and ZnCo-MOF after anneal

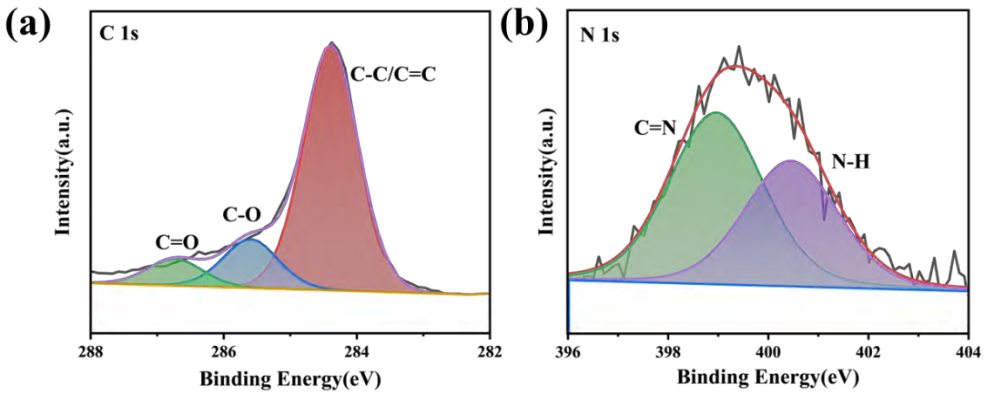

Fig. S8. XPS spectra of (a) C 1s, (b) N 1s.

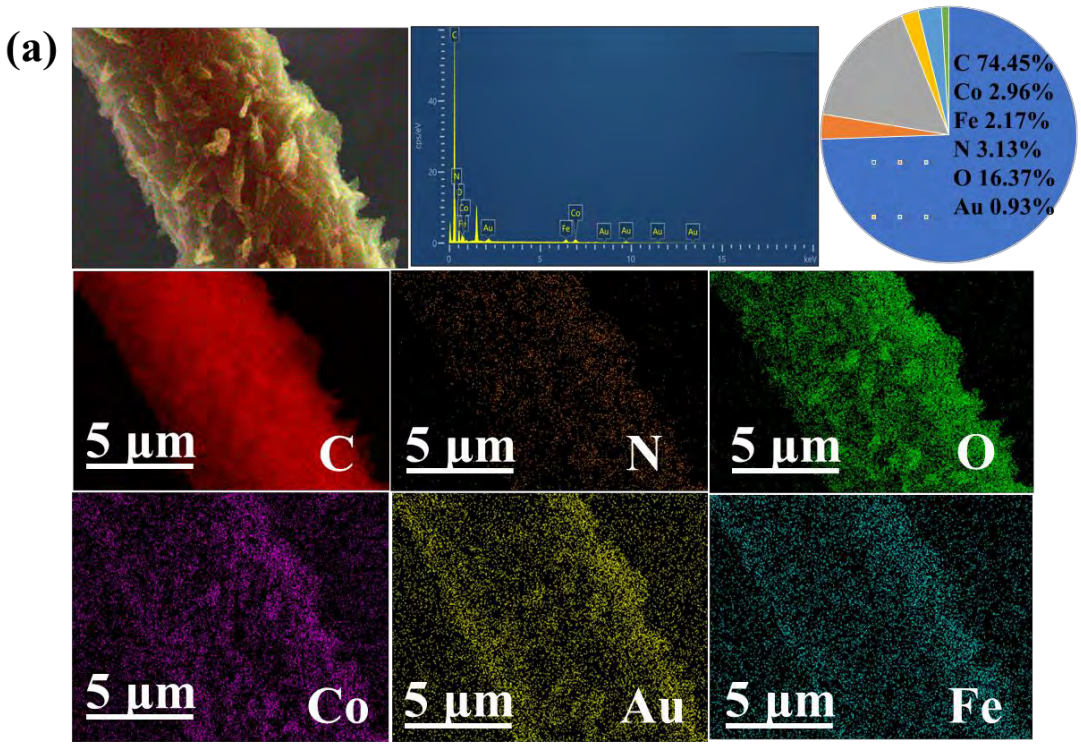

Fig. S9. (a) EDS elemental maps of FCO/Au/CPCN@CC; EDS C map, EDS N map, EDS O map, EDS Co map, EDS Au map, and EDS Fe map.

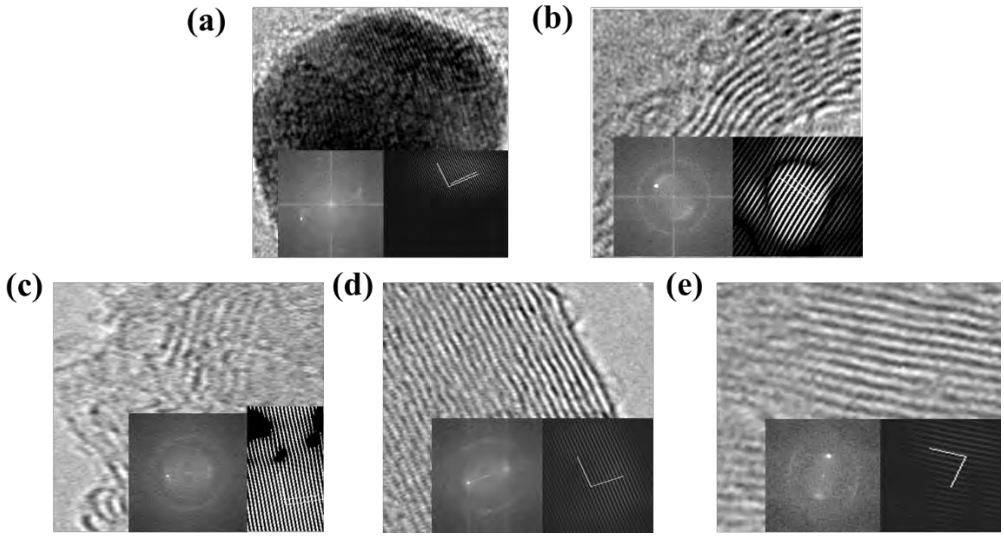

Fig. S10. (a) the lattice line, FFT and IFFT patterns of Au (111); (b) the lattice line, FFT and IFFT patterns of Co_3O_4 (111); (c) the lattice line, FFT and IFFT patterns of Co_3O_4 (311); (d) the lattice line, FFT and IFFT patterns of Fe_2O_3 (220); (e) the lattice line, FFT and IFFT patterns of Fe_2O_3 (104).

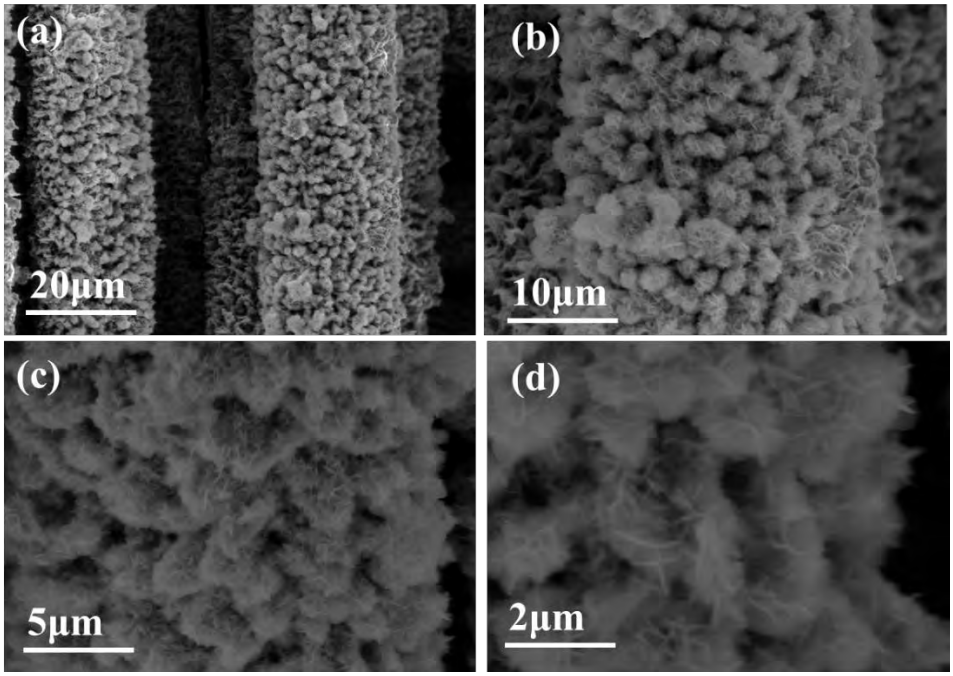

Fig. S11. SEM images of (a, b, c, d) FCO/Au/CPCN@CC after 10,000 cycles.

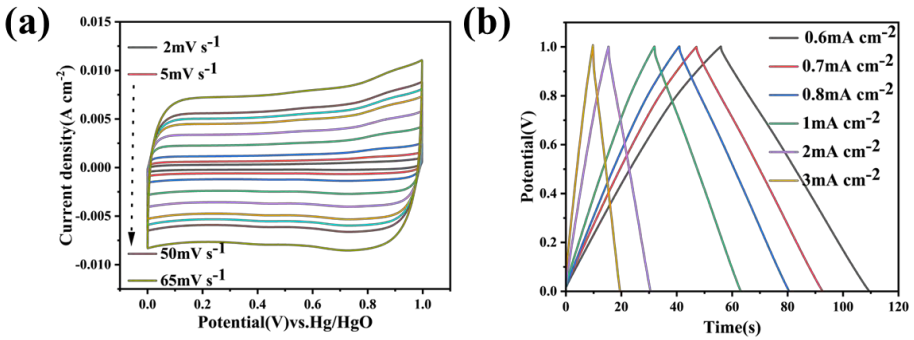

Fig. S12. (a) CV curves and (b) GCD curves of the AC electrode.

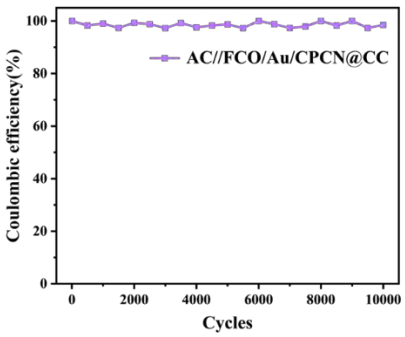

Fig. S13. Coulombic efficiency of AC//FCO/Au/CPCN@CC.

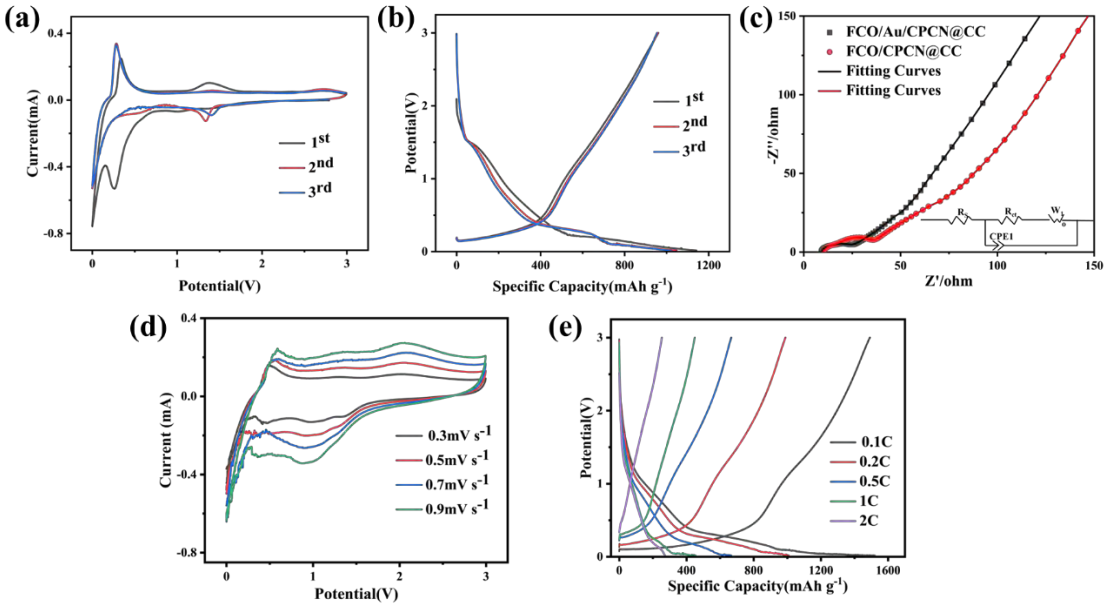

Fig. S14. (a) CV curves and (b) GCD profiles of FCO/CPCN@CC; (c) Nyquist plots curves of FCO/CPCN@CC and FCO/Au/CPCN@CC; (d) CV curves at different scanning rates and (e) GCD curves at different current densities of FCO/Au/CPCN@CC.

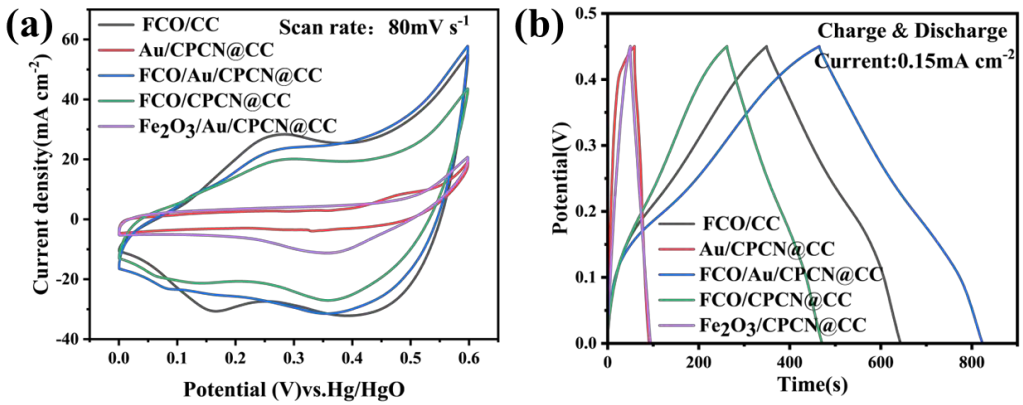

Fig. S15. (a) CV curves at 80 mV s^{-1} and (b) GCD curves at 0.15 mA cm^{-2} of FCO/CC, Au/CPCN@CC, FCO/Au/CPCN@CC, FCO/CPCN@CC, Fe_2O_3/CPCN@CC in 1M KOH solution.

Table S1. Specific capacitances, energy densities, and power densities of the hybrid asymmetrical supercapacitor at different current densities.

Electrodes	Current Densities ($mA\ cm^{-2}$)	Specific Capacitances ($F\ g^{-1}$)	Energy Densities ($W\ h\ kg^{-1}$)	Power Densities ($W\ h\ kg^{-1}$)
AC//FCO/Au/CPCN@CC	1	131.18	291.5	153.85
AC//FCO/Au/CPCN@CC	2	122.78	271.51	306.17
AC//FCO/Au/CPCN@CC	3	105.28	233.96	461.54
AC//FCO/Au/CPCN@CC	4	92.23	204.96	666.24
AC//FCO/Au/CPCN@CC	5	83.43	185.4	909.07
AC//FCO/Au/CPCN@CC	6	70.5	156.67	1200.03
AC//FCO/Au/CPCN@CC	7	65.15	144.78	1749.9

Table S2. EIS fitting parameters derived from the matching equivalent circuit.

samples	$R_s(\Omega)$	$R_{ct}(\Omega)$
Three-electrode system		
FCO/CPCN@CC	6.52	1.14
FCO/Au/CPCN@CC	5.81	0.42
Sodium-ion SCs		
AC//FCO/CPCN@CC	8.21	21.8
AC//FCO/Au/CPCN@CC	6.69	5.43
Sodium-ion battery		
FCO/CPCN@CC	9.7	26.65
FCO/Au/CPCN@CC	8.52	17.59

Table S3. Specific information on XPS spectra of different elements.

element	FWHM eV	Area(P) CPS.eV	Atomic %
Co	2.93	34026.39	7.6
Fe	6.14	17318.31	5.36
Au	2.83	2396.3	0.99
C	1.2	16970.22	61.95
N	2.2	6782.15	1.79
O	1.58	15723.35	22.31

References

[1] J. Li, G. Zan, Q. Wu, An ultra-high-performance anode material for supercapacitors: self-assembled long Co_3O_4 hollow tube network with multiple heteroatom (C-, N- and S-) doping, J. Mater. Chem. A 4(23) (2016) 9097-9105, https://doi.org/10.1039/c6ta02376b.

[2] A.V. Shinde, N.R. Chodankar, V.C. Lokhande, A.C. Lokhande, T. Ji, J.H. Kim, C.D. Lokhande, Highly energetic flexible all-solid-state asymmetric supercapacitor with Fe_2O_3 and CuO thin films, RSC Adv. 6(63) (2016) 58839-58843, https://doi.org/10.1039/c6ra11896h.

[3] F.I. Saaid, A. Arsyad, N.S.H. Azman, A. Kumar, C.-C. Yang, T.-Y. Tseng, T. Winie, The synergistic effect of iron cobaltite compare to its single oxides as cathode in supercapacitor, J. Electroceramics 44(3-4) (2020) 183-194, https://doi.org/10.1007/s10832-020-00209-4.

[4] M. Li, K.L. Zhu, H.X. Zhao, Z.Y. Meng, C.R. Wang, P.K. Chu, Construction of alpha-MnO_2 on Carbon Fibers Modified with Carbon Nanotubes for Ultrafast Flexible Supercapacitors in Ionic Liquid Electrolytes with Wide Voltage Windows, Nanomaterials 12(12) (2022) 2020, https://doi.org/10.3390/nano12122020.

[5] X. Wang, Y. Yang, F. Zhang, J. Tang, Z. Guo, Facile synthesis of Co_3O_4/CdO nanospheres as high rate performance supercapacitors, Mater. Lett. 261 (2020) 127141, https://doi.org/10.1016/j.matlet.2019.127141.

[6] K. Wang, J. Yang, J. Zhu, L. Li, Y. Liu, C. Zhang, T. Liu, General solution-processed formation of porous transition-metal oxides on exfoliated molybdenum disulfides for

high-performance asymmetric supercapacitors, J. Mater. Chem. A 5(22) (2017) 11236-11245, https://doi.org/10.1039/c7ta01457k.

[7] G. Sun, L. Ma, J. Ran, X. Shen, H. Tong, Incorporation of homogeneous Co_3O_4 into a nitrogen-doped carbon aerogel via a facile in situ synthesis method: implications for high performance asymmetric supercapacitors, J. Mater. Chem. A 4(24) (2016) 9542-9554, https://doi.org/10.1039/c6ta03884k.

[8] Z. Shi, L. Xing, Y. Liu, Y. Gao, J. Liu, A porous biomass-based sandwich-structured Co_3O_4@Carbon Fiber@Co_3O_4 composite for high-performance supercapacitors, Carbon 129 (2018) 819-825, https://doi.org/10.1016/j.carbon.2017.12.105.